International Journal of Rock Mechanics & Mining Sciences 206 (2026) 106643

Contents lists available at ScienceDirect

International Journal of Rock Mechanics and Mining Sciences

journal homepage: www.elsevier.com/locate/ijrmms

Research Paper

Modeling in-situ gas flow and coupled hydro-mechanical processes in the Opalinus Clay

Matthijs Nuus [a,*], Antonio Pio Rinaldi [a], Robert Cuss [b], Manuel Sentis [c], Bastian Graupner [c], Fabiano Magri [d,e], Frédéric Bernier [f]

[a] Swiss Seismological Service (SED) - ETH Zürich, Zürich, Switzerland
[b] British Geological Survey, Nottingham, UK
[c] Swiss Federal Inspectorate for Nuclear Safety (ENSI), Brugg, Switzerland
[d] Federal Office for the Safety of Nuclear Waste Management (BASE), Berlin, Germany
[e] Freie Universität Berlin, Berlin, Germany
[f] Federal Agency for Nuclear Control (FANC), Brussels, Belgium

ARTICLE INFO

Dataset link: Dataset for coupled hydro-mechanical modeling of gas flow in Opalinus Clay (GT experiment) (Original data)

Keywords:
Gas transport
Dilatant pathways
Hydro-mechanical coupling
Permeability
Opalinus Clay
GT-experiment

ABSTRACT

Deep geological repositories rely on low-permeability host rocks to ensure long-term containment of radioactive waste. The Opalinus Clay is considered a suitable host rock, acting as the primary geological barrier. Corrosion of waste containers under anoxic conditions produces hydrogen gas, which can accumulate due to the low permeability of the formation. Elevated gas pressures may exceed the minimum principal stress, potentially causing fracturing and compromising repository integrity. Since hydrogen generation will persist for more than 100,000 years, understanding gas transport mechanisms in low-permeability rocks is critical. Gas migration may occur through advective–diffusive flow, visco-capillary two-phase flow, dilatancy-controlled gas flow, or advective transport along macroscopic fractures. The dominant mechanism depends on gas pressure and rock microstructure, though controlling variables remain poorly constrained.

The GT (Gas Transport) experiment at the Mont Terri Rock Laboratory was conducted to study these processes by direct injection of helium into the Opalinus Clay in stepwise pressure increments until breakthrough occurred. Here, we present results of a coupled hydro-mechanical model using TOUGH-FLAC, linking multiphase flow simulations (TOUGH3) with geomechanics (FLAC3D). We aim to distinguish between gas transport mechanisms through different model configurations by fitting them to the observed pressure response, with emphasis on capturing the onset of dilatant pathways through permeability models. Our simulations reproduce observed injection pressures closely. The models allow investigation of conditions under which different gas transport mechanisms occur, particularly the onset of dilatant pathways. These results provide new insights into gas migration in the Opalinus Clay and its implications for repository safety.

1. Introduction

Deep geological repositories consist of natural and engineered barrier systems to prevent radionuclide transport into the biosphere.[1] The Opalinus Clay is currently proposed as the host rock to serve as a natural barrier for a nuclear waste repository in Switzerland due to several favorable properties, such as low permeability, potential for self-sealing of fractures,[2] and high sorption capacity.[3]

After closure of the repository, anoxic corrosion of canisters, steel in tunnel lining and other metallic waste forms result in the formation of gases, most notably hydrogen from steel.[4–6]

The anoxic corrosion reaction of carbon-steel is generally described by:

$$Fe + 2H_2O \rightarrow Fe(OH)_2 + H_2$$

Considerable gas pressure can build up within the repository as a result of the low permeability of the engineered and natural barriers. Gas can escape the repository through different transport mechanisms, which are generally subdivided into:

1. Advection and diffusion of dissolved gas
2. Two-phase flow

* Corresponding author.
E-mail address: matthijs.nuus@sed.ethz.ch (M. Nuus).

https://doi.org/10.1016/j.ijrmms.2026.106643
Received 10 April 2026; Received in revised form 13 June 2026; Accepted 12 July 2026
Available online 21 July 2026

3. Dilatancy controlled gas flow
4. Gas transport through fracturing

Which type of gas transport mechanisms dominates is largely controlled by the gas pressure[7] and the stress state. Gas transport through advection and diffusion occurs already at low pressures and is governed by Henry's and Fick's laws. Higher gas pressures increase gas solubility in pore water and thereby enhance diffusive transport. When gas pressure exceeds the gas entry pressure of the water-saturated rock, gas starts to displace porewater and two-phase flow, governed by a generalized form of Darcy's law, is initiated. Dilatancy controlled gas flow is believed to occur when gas pressure approaches or exceeds the minimum principal stress creating self-healing micro-fractures and thereby increasing the intrinsic permeability. When the gas pressure exceeds the sum of the minimum principal stress and tensile strength of the rock, macroscopic fractures might be formed along which single-phase gas flow occurs. Additional factors that influence which of these gas transport mechanisms occur or dominate are hydraulic and mechanical properties of the barriers and the hydromechanical state of the rock.[8]

Significant uncertainties persist regarding gas transport mechanisms in compact clays, such as the Opalinus Clay. Given the gas pressure expected due to corrosion of metal canisters in a deep geological repository, conventional theory suggests that hydrogen is transported through the clay barrier using two-phase flow.[1] In contrary, Harrington and Horseman[9] suggest reliance on conventional two-phase flow theory is inadvisable for initially saturated compact clays. Due to the extremely narrow interparticle spaces, the capillary threshold needed for gas to displace porewater is simply too large. Lab-scale experimental results suggest that gas does not occupy or flow through intergranular pores of the clay matrix, but rather through pressure-induced dilatant pathways that partially close after the gas pressure falls. If gas fails to escape the low-permeability host rock through either two-phase flow or dilatancy controlled gas flow, gas pressure could build up high enough to lead to the formation of macroscopic tensile fractures. This poses a risk to the structural integrity of the repository and could result in the release of radionuclides into the biosphere.

The understanding of gas transport mechanisms in water-saturated clay rocks is still not complete. This study therefore aims to characterize the physical phenomena describing gas transport and its mechanical interaction with the surrounding barriers. This is achieved by constructing and evaluating a 3D-coupled hydro-mechanical model of an in-situ gas injection experiment. Hydro-mechanical simulations were carried out using TOUGH-FLAC, a code that couples the multi-phase flow simulator TOUGH3 with the geomechanical simulator FLAC3D.[10] The in-situ experiment that was simulated is called the Gas Transport (GT) experiment, which was conducted in the Mont Terri Rock Laboratory in Switzerland. During the experiment, helium was injected for over a year into the Opalinus Clay while the pressure and mechanical response around the injection interval were continuously monitored. Helium, in this context, is used as a proxy gas to represent hydrogen that would be generated around a deep geological repository, and was chosen to minimize geochemical alteration that could arise with hydrogen. In the hydro-mechanical model, we aim to recreate the pressure response in the injection interval and compare the measured and modeled deformation responses. Using the coupled model, we can account for different gas-transport mechanisms, with a focus on the onset of dilatant pathways, which will be modeled using two different approaches.

2. GT-experiment

The Gas Transport (GT) experiment comprises both laboratory and in-situ components aimed at evaluating gas transport models and the behavior of clay rocks under gas pressure. This study focuses on the in-situ experiment, which was conducted in the Mont Terri Rock Laboratory, which lies at a depth of 280 m below the surface within the Opalinus Clay.[11] The bedding of the Opalinus Clay at the GT-experiment site dips 33° toward the southeast, with a dip direction of approximately 140°. The Opalinus Clay can be subdivided into three lithofacies: sandy, carbonate-rich, and shaly facies. The GT-experiment is located within the shaly facies (Fig. 1).

The main description of the experimental setup as well as the experimental results can be found in Cuss et al..[13] In brief, the in-situ experiment consists of a central injection borehole surrounded by eight observation boreholes, which are drilled with a dip of 57° in order to be perpendicular to the bedding. The observation boreholes, drilled parallel to the injection borehole, are arranged in a circle with a 1 m radius around the injection borehole (Fig. 2). All boreholes are equipped with fiber optic (FO) cables to measure deformation, with the cables either cemented in place or clamped to the packer system. Additionally, two observation boreholes are equipped with chain extensometers, one observation borehole is equipped with a chain extensometer and an inclinometer, and one observation borehole is equipped with a 6-fold packer system containing pressure sensors. The injection borehole is equipped with a 3-fold packer system containing interval access lines going into the injection interval and pressure sensors. All boreholes are ~15 m long, with the exception of the pore pressure borehole which is ~20 m long.

The surface equipment consists of a high-precision syringe pump (ISCO-500 series D) which pumps water into a pressure vessel filled with helium. The syringe pump has a volume of 500 ml and is connected to a second pressure vessel with water for refilling purposes. The pressure vessel filled with helium has a volume of approximately 5000 ml and can be refilled through a connected gas tank. Three electric valves control the refilling of the different tanks. Pressure sensors are integrated along the injection lines to monitor the injection pressure at the surface (Fig. 3).

Prior to the injection of helium, hydraulic testing was carried out at the pore pressure borehole (BGT-2) and the injection borehole (BGT-10) (Fig. 2, Top view). Hydraulic testing at BGT-2 was conducted to estimate the transmissivity and hydraulic head at all six intervals before and after the surrounding boreholes were drilled, in order to verify that the boreholes were spaced sufficiently far apart to avoid significant cross-hole hydraulic responses between BGT-2 and BGT-10. After the remaining boreholes were drilled, no noticeable change in transmissivity and hydraulic head were observed in BGT-2. Hydraulic testing consisted of both pulse injection tests and constant head injections. Hydraulic conductivity values estimated from constant head injections range from 2.6×10^{-13} to 3.17×10^{-13} m/s for the injection and pore pressure observation boreholes. The equivalent permeability of the injection interval is approximately 2.96×10^{-20} m^2, assuming a pore water viscosity and density of 1.1373×10^{-3} Pa s and 1020 kg/m^3, respectively.

Helium injection began in July 2022 and lasted until September 2023. During the first two months, the injection rates were kept relatively low, and the pressure level was maintained at the same level as it was prior to gas injection to ensure that all the water in the injection interval was displaced by helium. The injection protocol aimed to increase the pressure in increments of approximately 0.5 MPa over periods of about two weeks. Each pressure increment was followed by an equally long period during which the pressure was maintained at a constant level. The resulting experimental pressure evolution during the helium injection phase is shown in Fig. 4. This step-wise pressure increase pattern continued until a pressure of approximately 4.2 MPa was reached in May 2023, at which point a sudden pressure drop of approximately 0.9 MPa was observed in the injection interval. Explaining the origin of this first experimentally observed pressure drop is the primary focus of the present study. After the pressure stabilized at around 3.2 MPa in June 2023, it was slowly increased until it reached a value of around 3.7 MPa by the end of August 2023, after which the pressure dropped by almost 2.5 MPa. The injection was then stopped.

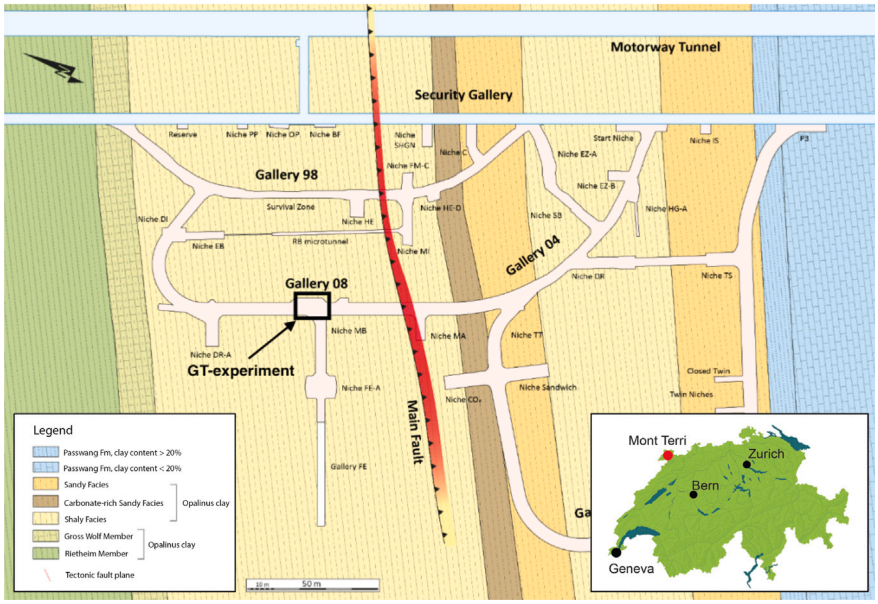

Fig. 1. Map of the Mont Terri Rock Laboratory showing different formations and facies, galleries and niches, the main fault and the location of the GT-experiment. Modified after Mont Terri Project.[12]

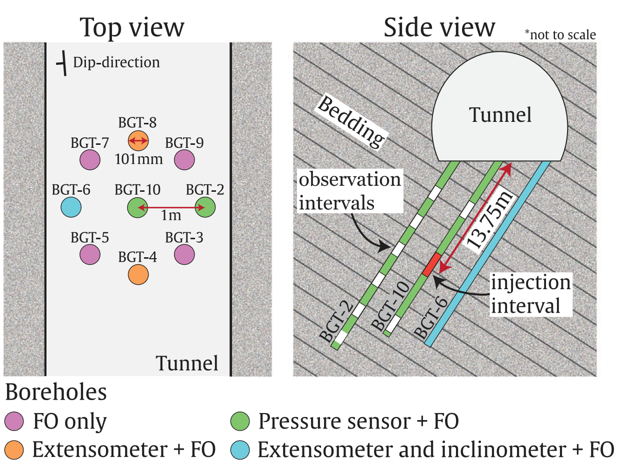

Fig. 2. Arrangement of injection and observation boreholes.

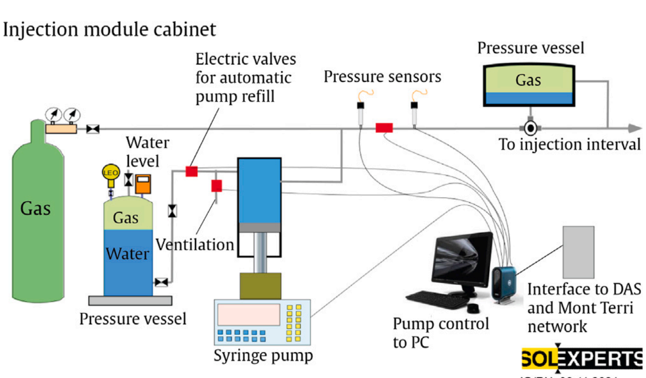

Fig. 3. Schematic layout of surface equipment.

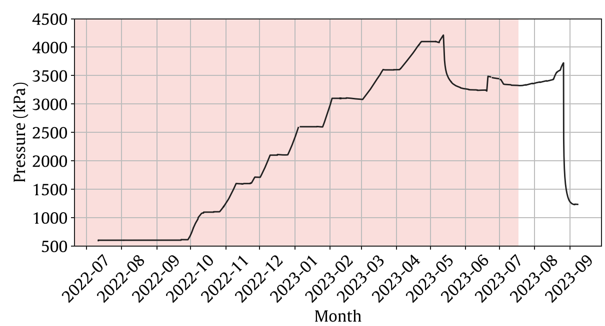

Fig. 4. Pressure evolution measured in the injection interval of borehole BGT-10. The time frame focused on in this study is highlighted in red. (For interpretation of the references to color in this figure legend, the reader is referred to the web version of this article.)

3. Modeling approach

3.1. Fluid flow model (TOUGH3)

The fluid flow model is created in TOUGH3: a numerical simulator that solves mass and energy balance equations for fluid flow for multi-phase and multi-component systems.[14] The mass balance equation for fluid component κ can be written in the following general form:

$$\frac{d}{dt}\int_{V_n} M^{\kappa}\, dV_n = \int_{\Gamma_n} \boldsymbol{F}^{\kappa} \cdot \boldsymbol{n}\, d\Gamma_n + \int_{V_n} q^{\kappa}\, dV_n \tag{1}$$

The first term of the equation above is the mass accumulation term showing the change of mass M^{κ} within an element of volume V_n. The second term is the flow term which calculates the flux F^{κ} between elements across interface Γ_n. The third term contains sinks and sources q^{κ}. The advective mass flux, $\mathbf{F}^{\kappa}_{adv}$, is the sum of the phase fluxes:

$$\mathbf{F}^{\kappa}_{adv} = \sum_{\beta} X^{\kappa}_{\beta} \mathbf{F}_{\beta} \tag{2}$$

in which X^{κ}_{β} is the mass fraction of component κ in phase β and where the individual phase fluxes, $\mathbf{F}_{\beta}$, are given by a multiphase version of

Darcy's law:

$$\mathbf{F}_\beta = \rho_\beta \mathbf{u}_\beta = -k\frac{k_{r\beta}\rho_\beta}{\mu_\beta}\left(\nabla P_\beta - \rho_\beta \mathbf{g}\right) \tag{3}$$

in which ρ_β is the density, $\mathbf{u}_\beta$ is the Darcy velocity, k is the intrinsic permeability, $k_{r\beta}$ is the relative permeability, μ_β is the viscosity, $\mathbf{g}$ is the acceleration of gravity and P_β is the fluid pressure of phase β, which is defined as:

$$P_\beta = P + P_{c\beta} \tag{4}$$

where P is the pressure of the gas phase and $P_{c\beta}$ is the capillary pressure.[14]

In this study, we use the van Genuchten function[15] to describe the relationship between capillary pressure and saturation. The relationship is described as follows:

$$P_c = -\frac{1}{\alpha}\left[\left(S_{el}^{-1/m}\right) - 1\right]^{1/n} \tag{5}$$

in which n is the Van Genuchten pore size distribution index parameter, $m = 1 - 1/n$, $1/\alpha$ is the apparent gas entry pressure, S_{el} is the effective liquid saturation, which is defined as:

$$S_{el} = \frac{S_l - S_{lr}}{1 - S_{lr}} \tag{6}$$

in which S_l is the liquid saturation and S_{lr} is the residual water saturation.

The relative permeability for the water k_{rl} and gas phase k_{rg} (Eq. (3)) are described using a modified version of the Van Genuchten model[16], and has the following form:

$$k_{rl} = S_{el}^{\frac{1}{2}}\left[1 - (1 - S_{el}^{1/m})^m\right]^2 \tag{7}$$

$$k_{rg} = \left(1 - S_{eg}\right)^{\frac{1}{3}}\left[1 - S_{eg}^{1/m}\right]^{2m} \tag{8}$$

in which S_{eg} is the effective gas saturation:

$$S_{eg} = \frac{S_l}{1 - S_{gr}} \tag{9}$$

where S_{gr} is the residual gas saturation. To solve the mass balance equation (Eq. (1)), TOUGH3 employs an integral finite-difference method for spatial discretization and a first-order fully implicit scheme for time integration.

The hydraulic parameters used to represent Opalinus Clay are shown in Table 1. The permeability parallel and perpendicular to bedding are based on values reported in NAGRA,[17] as the permeability parallel to bedding has a similar value to the permeability measured during the constant head (HI) injection test. The remaining hydraulic parameters, including the van Genuchten parameters, are also based on data reported in NAGRA.[17]

The van Genuchten curves for capillary pressure and relative permeability are shown in Fig. 5. In NAGRA,[17] the apparent gas entry pressure is reported as 34 MPa, which is adopted here as the reference value. However, for model calibration purposes, this value was increased to 60 MPa. This required adjustment is related to differences in the implementation of the gas relative permeability function. In the formulation used by NAGRA,[17] a different definition of effective gas saturation is used compared to the formulation implemented in TOUGH3 (Eq. (9)). As a result, the gas phase remains less mobile at low gas saturations than in the TOUGH3 implementation. Consequently, a higher apparent gas entry pressure was required to reproduce the observed pressure evolution.

TOUGH3 uses different equation of states (EOS), which link primary variables and secondary parameters to determine phase state and phase composition. In this study we use EOS5[14], which is the fluid property module for water and hydrogen. To account for the different viscosity and molar mass of hydrogen compared to the injected helium, we adjust those parameters in the source code.

Table 1
Hydraulic parameters for Opalinus Clay used in TOUGH3.

Parameter	Symbol	Value	Unit
Intrinsic permeability (parallel to bedding)[a]	$k_\parallel$	5×10^{-20}	m^2
Intrinsic permeability (perpendicular to bedding)[a]	$k_\perp$	1×10^{-20}	m^2
Porosity[a]	ϕ	0.16	–
Density[a]	ρ	2500	kg/m^3
van Genuchten parameter[a]	n	1.67	–
Apparent gas entry pressure[b]	$1/\alpha$	6×10^7	Pa
Saturation (wetting phase)[a]	S_{ls}	1.0	–
Residual liquid saturation[a]	S_{lr}	0.01	–
Residual gas saturation[a]	S_{gr}	0.0	–

[a] Parameters taken from NAGRA.[17]
[b] Adjusted for fitting purposes.

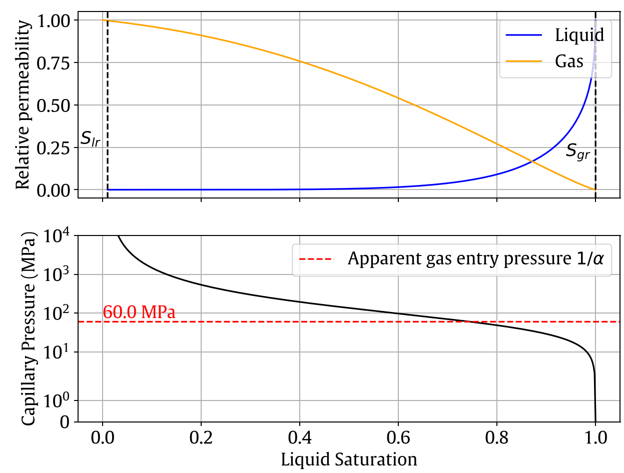

Fig. 5. Capillary pressure and relative permeability curves according to Van Genuchten formulation.

3.2. Geomechanical model (FLAC3D)

For the geomechanical coupling with TOUGH3, we use FLAC3D. In FLAC3D, the mechanical equilibrium is calculated using the momentum equation:

$$\sigma_{ij,j} + \rho b_i = \rho\frac{dv_i}{dt} \tag{10}$$

where $\sigma_{ij,j}$ is the divergence of the stress tensor, b_i is the vector of body forces per unit mass, ρ is the rock density, and dv_i/dt is the material derivative of the velocity.[18]

The total stress σ is affected by fluid flow through Biot's theory of poroelasticity[19]:

$$\sigma_{ij} = \sigma'_{ij} - \alpha p \delta_{ij} \tag{11}$$

where σ' is the effective stress, α is Biot's coefficient, δ_{ij} is the Kronecker delta and p is the pore pressure transferred from TOUGH3.

Numerous constitutive models to describe the stress–strain relationship can be implemented using FLAC3D. In this study, we use the ubiquitous joint model with strain softening (SUBI), which accounts for the presence of an orientation of weakness (weak plane) in a Mohr–Coulomb model. This weak plane represents the bedding of the Opalinus Clay. Strain-change is calculated from stress-change using Hooke's law in the elastic domain. The criterion for failure on the plane, whose orientation represents the bedding strike and dip of the Opalinus Clay, is determined by a Mohr–Coulomb envelope with tension cutoff.[18] The failure envelope of the weak plane distinguishes between shear and tensile failure, and is expressed as:

$$f^s = \tau + \sigma_{3'3'} \tan\phi_j - c_j = 0 \tag{12}$$

for shear failure, and

$$f^t = \sigma_{3'3'} - \sigma_j^t = 0 \tag{13}$$

for tensile failure. Here, the subscript j denotes properties of the weak plane, where ϕ_j is the friction angle, c_j is the cohesion, and σ_j^t is the tensile strength. Furthermore, $\sigma_{3'3'}$ is the normal traction component acting on the weak plane and τ is the tangential traction component acting on the weak plane, defined as:

$$\tau = \sqrt{\sigma_{1'3'}^2 + \sigma_{2'3'}^2}. \tag{14}$$

Once the failure criteria have been met, the plastic strain increment $\Delta\epsilon_i^p$ can be calculated using the flow rule:

$$\Delta\epsilon_i^p = \lambda \frac{\partial g}{\partial \sigma_{ij}} \tag{15}$$

in which λ is a plastic multiplier and g is the flow potential. The flow potentials for shear- g^s and tensile-plastic flow g^t for the weak plane are defined respectively as:

$$g^s = \tau + \sigma_{3'3'} \tan\psi_j \tag{16}$$

$$g^t = \sigma_{3'3'} \tag{17}$$

in which ψ_j is the dilation angle of the weak plane and τ and $\sigma_{3'3'}$ are the tangential and normal traction components on the plane. Mechanical equilibrium or steady plastic flow is computed using the finite-difference approach implemented in FLAC3D.

A similar failure and plastic strain flow formulation is used for the intact rock matrix. The difference is that its material properties, such as cohesion, friction angle, and dilation angle, differ from those of the weak plane. Both the matrix and the weak plane are governed by a Mohr–Coulomb failure criterion with a tension cutoff, but their strength and deformation behaviors reflect these differing parameters.

The key distinction between a standard Mohr–Coulomb model and a Mohr–Coulomb model with strain-softening is that the latter permits the softening of cohesion, friction angle, dilation angle, and tensile strength after plastic yield begins.[18] In our model, only the friction angle of the weak plane was allowed to soften to its residual value as a function of accumulated plastic strain. Because the weak-plane failure criterion used to represent the onset of dilatant pathways uses zero cohesion and therefore zero tensile strength, no further cohesion or tensile-strength softening can occur. Similarly, the dilation angle assigned to the bedding planes was set to 0°, meaning that no further dilation softening can occur. The strain-softening behavior therefore only affects the frictional resistance of the weak plane.

The mechanical parameters for the matrix are taken from NAGRA[20,21] (Table 2), while the principal stress magnitudes and orientations are based on ranges compiled from previous studies by Guglielmi et al..[22] To simplify implementation in our model, we assume that the principal stresses are perfectly vertical and horizontal, following a similar approach to Amann et al..[23] The adopted values, along with the reported stress ranges, are summarized in Table 3. The average of the stress tensor ranges, our assumed stress tensor orientations, and the bedding orientation are shown in a stereonet (Fig. 6). Since the injection occurs approximately 11.5 m below the gallery floor, the stress magnitudes must be adjusted accordingly. These adaptations, including the calculation of stress gradients, are discussed in detail in Section 3.4.3.

The failure parameters for the bedding plane (Table 2) are calibrated so that the onset of failure coincides with the moment the pressure drop from 4.2 MPa to 3.3 MPa is observed (Fig. 4). In practice, we identify the failure criterion that triggers after an effective-stress reduction corresponding to the pore-pressure increase accumulated prior to the pressure drop, as illustrated by the stress-path evolution in the Mohr-circle representation (Fig. 7). The resulting bedding-plane failure envelope does not necessarily represent peak shear strength

Table 2
Material parameters for Opalinus Clay used in FLAC3D.

Parameter	Symbol	Value	Unit
Young's modulus[a]	E	7×10^9	Pa
Poisson's ratio[a]	ν	0.27	–
Cohesion[a]	c	3.1×10^6	Pa
Friction angle[a]	φ	29	°
Dilation angle[a]	ψ	0	°
Tensile strength[a]	σ^t	0.5×10^6	Pa
Biot coefficient[a]	α	1	–
Cohesion (joint)[b]	c_j	0	Pa
Dilation angle (joint)[b]	ψ_j	0	°
Friction angle (joint)[b]	φ_j	17.3	°
Residual friction angle (joint)[b]	φ_{jr}	13.7	°
Tensile strength (joint)[b]	σ_j^t	0	Pa
Lithostatic stress gradient[c]	–	25×10^3	Pa/m

[a] Parameters taken from NAGRA.[20,21]
[b] Empirically determined parameters for onset of dilatancy criteria.
[c] Based on mean bulk density overlying layers at Mont Terri.[24]

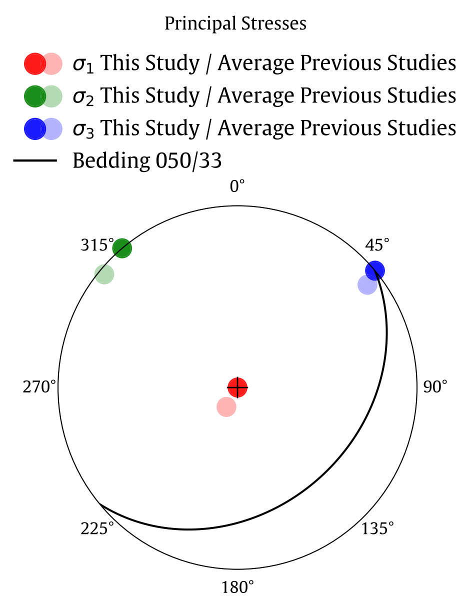

Fig. 6. Stereonet showing the orientations of the average principal stresses based on Guglielmi et al.[22] and those applied in the model. The black line indicates the strike and dip of the bedding plane.

but, in this case, rather marks the onset of dilatancy or micro-crack development, which would lead to an increase in permeability. This explains why our chosen friction angle and cohesion for the bedding plane are slightly lower than values reported in the literature, where friction angles of 19° with a cohesion of 1.7 MPa[25] and 21° with a peak cohesion of 0.9 MPa[26–28] have been proposed. In contrast, our model is cohesionless and it uses a friction angle of 17.3°.

3.3. Coupling and permeability modifications

FLAC3D and TOUGH3 are coupled at every time step.[10] The next step in the modeling process is only initiated once TOUGH3 has reached convergence and mechanical equilibrium is achieved in FLAC3D. Between each time step, pressure, permeability, and porosity are exchanged between the two codes. In our case, we assume isothermal conditions, so temperature is not part of the coupling. The fluid pressure calculated in TOUGH3 is transferred to FLAC3D, where it influences the stress state and thereby drives deformation. Porosity and permeability can also be updated at each time step based on different constitutive models. When dilatancy of the Opalinus Clay begins and gas starts to propagate through localized dilatant pathways, the permeability of the

Table 3
Ranges and assumed values of principal stresses at Mont Terri, based on Guglielmi et al..[22]

Principal Stress	Range (Azimuth/Dip)	This Study (Azimuth/Dip)	Magnitude Range (MPa)	This Study Magnitude (MPa)
σ_1	N210–N315/70°–90°	N000/90°	6–7	6.5
σ_2	N310–N055/00°–07°	N320/00°	4–5	4.5
σ_3	N040–N052/00°–18°	N050/00°	0.6–2.9	2.9

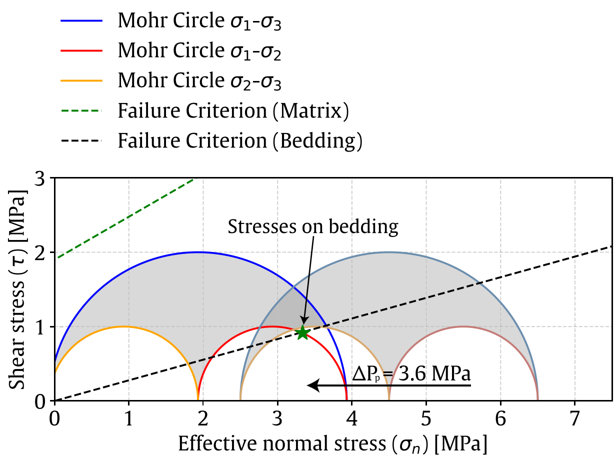

Fig. 7. Mohr Circle shift due to increased pore pressure and failure envelopes for the matrix and the bedding.

Table 4
Parameters for permeability modification.

Parameter	Symbol	Value	Unit
Threshold pressure	p_{th}	4.2×10^6	Pa
Empirical constant before threshold	$\mathbf{a}_1$	$\begin{bmatrix}1\\1\\0\end{bmatrix}$	–
Empirical constant after threshold	$\mathbf{a}_2$	$\begin{bmatrix}92\\92\\18.4\end{bmatrix}$	–
Failure permeability	k_f	5×10^{-19}	m^2
Empirical elastic constant	$\mathbf{b}_1$	$\begin{bmatrix}50\\50\\10\end{bmatrix}$	–
Empirical plastic constant	$\mathbf{b}_2$	$\begin{bmatrix}27000\\27000\\5400\end{bmatrix}$	–

material increases rapidly. To capture this behavior, permeability must be treated as a dynamic variable in the model. In our simulations, we apply two different approaches to modify permeability in response to evolving gas pressure and deformation.

The first approach calculates permeability directly as a function of gas pressure.[20,29,30] In this approach, permeability increases suddenly once the gas pressure exceeds a defined threshold value. Below this threshold, permeability remains relatively constant, while above the threshold, it increases in proportion to the difference between gas pressure and the threshold value. This pressure-based permeability modification is expressed as follows:

$$k = (1 + a_1) \cdot p_g \cdot k_{\text{ini}} \quad \text{if } p_g \le p_{\text{th}} \tag{18}$$

$$k = a_2 \cdot (p_g - p_{\text{th}}) + (1 + a_1 \cdot p_{\text{th}}) \cdot k_{\text{ini}} \quad \text{if } p_g > p_{\text{th}} \tag{19}$$

where k is the updated permeability of the element, k_{ini} is the initial intrinsic permeability, p_g is the gas pressure, and p_{th} is the pressure threshold that marks the onset of rapid permeability change. The parameters a_1 and a_2 are empirical constants that control the magnitude of the permeability adjustment before and after the threshold is crossed (Table 4).

In the second approach, permeability is updated based on both elastic and plastic strains within the material.[30] Here, the onset of plastic deformation leads to a sudden increase in permeability, making the mechanical response of the material a key driver of permeability evolution. The permeability update function in this strain-based approach is given by:

$$\mathbf{k} = 10^{\mathbf{b}_1 \cdot \varepsilon_{\text{vol}}} \cdot \exp^{\mathbf{b}_2 \cdot \varepsilon^p} \cdot \mathbf{k}_{\text{ini}} \tag{20}$$

$$k_{\text{ini},\parallel} = \begin{cases} k_{\text{ini}} & \text{if } \varepsilon^p = 0 \\ k_f & \text{if } \varepsilon^p > 0 \end{cases} \qquad k_{\text{ini},\perp} = \begin{cases} k_{\text{ini}} & \text{if } \varepsilon^p = 0 \\ 0.2 \times k_f & \text{if } \varepsilon^p > 0 \end{cases} \tag{21}$$

In this equation, ε_{vol} represents the volumetric strain, ε^p is the plastic strain, and $\mathbf{b}_1$ and $\mathbf{b}_2$ are empirical constants that control the sensitivity of permeability to volumetric and plastic strain, respectively. As soon as the plastic strain exceeds zero in an element, we set the initial permeability ($\mathbf{k}_{\text{ini}}$) of that element in Eq. (20) to a chosen failure permeability (k_f in Eq. (21), Table 4). The empirical constants b_1 and b_2 are defined as vectors to allow for anisotropic permeability evolution, enabling a greater increase in permeability parallel to the bedding compared to the perpendicular direction. As volumetric strain increases, the pore space expands, leading to higher permeability, while the onset of plastic strain can trigger a more significant permeability enhancement. By incorporating these strain-based mechanisms, this approach provides a more direct linkage between mechanical deformation and permeability changes, reflecting the physical processes underlying dilatant gas flow.

To account for poro-elastic effects, we update porosity as a function of pore pressure using the porosity increment formulation implemented in the TOUGH3–FLAC3D coupling[10]:

$$d\phi = A(\alpha, \phi, K)\ dp\ +\ \Delta\phi, \tag{22}$$

in which $A(\alpha, \phi, K)$ describes the poro-elastic response through the Biot coefficient α, the drained bulk modulus K, and the current porosity ϕ, and a porosity correction term $\Delta\phi$ accounting for mechanical deformation. This porosity update is applied in both model approaches where permeability is also modified. A complete derivation and detailed description of the terms in Eq. (22) is given by Kim et al..[31]

3.4. Model set-up

3.4.1. Model geometry and mesh

A mesh representing the GT-experiment was generated using GMSH.[32] The model consists of an outer cube measuring $14 \times 14 \times 8$ m, with a nested tilted inner cube of $5 \times 5 \times 2.5$ m (Fig. 8). The outer cube is oriented such that its faces are aligned with the three principal stress directions (i.e. the lateral faces align with the horizontal principal stresses and the top with the vertical principal stress; Fig. 6). The inner cube shares the same horizontal orientation as the outer cube, but is tilted by 33° to represent the bedding dip of the Opalinus Clay. The inner cube is built up of 18 layers, each tilted in the same direction as the cube. A cylinder, also inclined at 33°, is positioned at the center of the inner cube and spans its full height. This cylinder

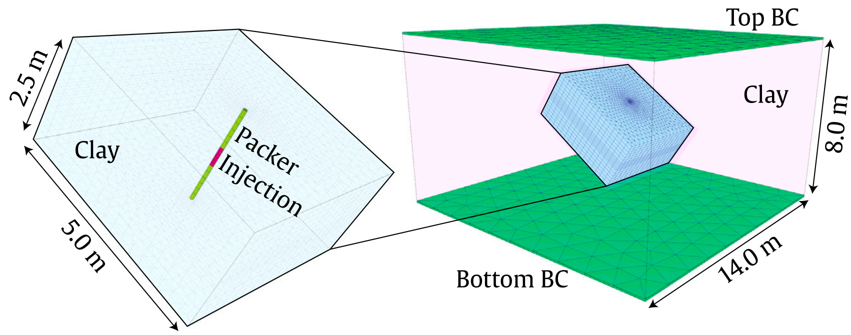

Fig. 8. 3D mesh of the GT-experiment, showing the geometry and dimensions of the model and the different assigned materials.

has a diameter of 0.11 m and represents the injection borehole used in the in situ experiment. The top and bottom 1 m segments of the cylinder correspond to the packers, while the central 0.5 m represents the injection interval. Each packer section is subdivided into 6 prismatic layers, as is the injection interval, resulting in 18 layers in total across the borehole height. The model includes five material zones: injection, clay, top boundary, bottom boundary, and packers. Two mesh types are used: prismatic elements for the inner domain and tetrahedral elements for the outer domain. The inner tilted cube is discretized using 27 936 prismatic elements, while the outer cube consists of 36 862 tetrahedral elements. This layered prism structure ensures that element connections within each layer maintain an orientation of 33°, while connections between adjacent layers consistently form an angle of 57°.

This setup was chosen for two key reasons. First, the prismatic mesh in the inner tilted cube enables a straightforward assignment of permeability anisotropy in TOUGH3: bedding-parallel permeability is applied to connections within layers, and bedding-perpendicular permeability to those between layers. The geometry reflects the bedding structure of the Opalinus Clay while still respecting the vertical gravity direction.

Second, the axis-aligned outer cube allows fixed pressure boundary conditions to be applied at the top and bottom of the domain in TOUGH3 for a specific depth, without requiring rotation of the gravity vector. In FLAC3D, it also simplifies the application of the principal stress tensor and its associated stress gradients, as no stress tensor rotation is necessary, since we assume that the principal stresses are perfectly vertical and horizontal (Fig. 6). While no permeability anisotropy is assigned in the outer domain, the inner tilted cube is sufficiently large to restrict fluid flow into the outer region, ensuring that the boundary conditions and mechanical assumptions remain valid.

3.4.2. Hydraulic boundary conditions and initialization

The hydraulic parameters listed in Table 1 for the TOUGH3 model are those used for the clay material. The other materials share the same parameters, except for porosity, permeability, and the capillary pressure and relative permeability functions. The porosity for the injection interval is set to 0.602, chosen such that the sum of the volumes of all injection elements multiplied by this porosity equals the measured volume of water (2.1 L) needed to fill the interval. We set the capillary pressure in the injection interval to a constant value of 0 and assume that all phases are perfectly mobile, thereby preventing water from (re-)entering the injection interval once it is fully saturated with helium at the beginning of the gas injection simulation. The permeability of the injection interval is set to 1×10^{-16} m^2, while the packer elements are assigned the same horizontal permeability as the clay but a vertical permeability reduced by two orders of magnitude to 1×10^{-22} m^2.

The top and bottom boundaries are implemented to enforce fixed pressure conditions in the TOUGH3 model. At the start of the simulation, a hydrostatic pressure gradient is assumed. The boundary pressure values are calculated based on this gradient and the measured pressure in the interval of the observation borehole BGT-2, which is at the same depth as the injection interval in the injection borehole BGT-10 (Fig. 2). This interval pressure is 0.65 MPa. Using this reference value, the top and bottom boundary conditions are set to 0.61 MPa and 0.69 MPa, respectively, corresponding to positions 4 m above and below the injection interval. These values are then held constant throughout the simulation.

In addition, no-flow boundary conditions are applied to all other sides in the TOUGH3 model. An initial run with a fully saturated domain to steady-state ensures stable initial conditions.

3.4.3. Mechanical boundary conditions and initialization

To initialize the appropriate stress conditions, a steady-state geomechanical model is first run in FLAC3D. The principal stresses are applied directly to outer faces of the mesh (Fig. 9).

In the model, the vertical stress is applied as a fixed value on the top face of the domain. The horizontal stress gradients are imposed on the respective side boundaries, which are aligned with the principal stress orientations. The bottom boundary is defined with a roller condition, allowing tangential movement while constraining displacement normal to the surface (Fig. 9).

The principal stress magnitudes are estimated based on previous measurements at the Mont Terri underground laboratory at gallery depth (Table 3; Guglielmi et al.[22]). However, since the injection experiment is located 11.5 m below the gallery floor, this depth difference must be accounted for. A lithostatic stress gradient of 0.025 MPa/m (Table 4; Sciandra et al.[24]) is used to compute the vertical stress at the depth of the injection interval. Assuming that the principal stress ratio remain constant with depth and that the orientation of the stress tensor does not change, the corresponding horizontal stress gradients are 0.011 MPa/m for σ_h and 0.017 MPa/m for σ_H. These gradients are applied as linearly varying boundary conditions, ensuring that the horizontal stress state evolves correctly with depth within the domain.

3.4.4. Simulation of helium injection rates using a tank model

Helium injection rates were not directly recorded by the surface equipment (Fig. 3). Instead, the recorded change in water volume within the syringe pump was used to estimate the helium injection rates by means of a TOUGH3 pressure-vessel model (Fig. 10). The model consists of two elements with volumes of 5.0 L and 2.1 L, representing the pressure vessel and the measured volume of the injection interval, respectively.

The pressure vessel is initially fully saturated with helium, and it is assumed that after the first two months of gas injection the injection interval was also fully occupied by helium. A capillary pressure relationship was implemented to ensure that only helium could migrate into the injection interval. The changing water volume in the syringe pump was converted into a water injection rate into the pressure vessel, resulting in displacement of helium across the interface between the pressure vessel and the injection interval. The resulting helium injection rate depends not only on the water injection rate into the pressure vessel, but also on the amount of helium remaining within the vessel. It was therefore necessary to account for periods during which the pressure vessel was refilled with helium in order to estimate the helium injection rates as accurately as possible.

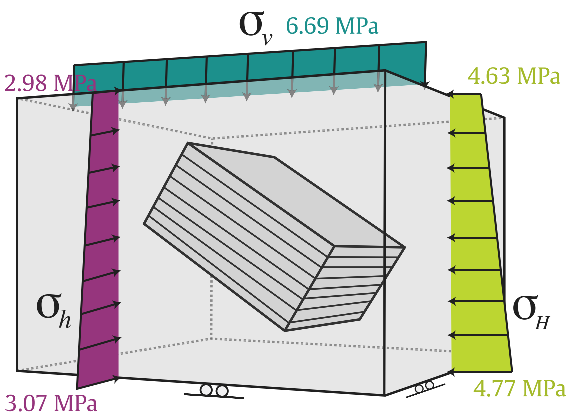

Fig. 9. Applied stress boundary conditions on the model domain. Stress gradients are applied to both horizontal stresses, while a fixed vertical stress is imposed at the top of the model. Numbers indicate the imposed stress values at the top and bottom of the model domain. The bottom boundary is constrained with roller boundary conditions.

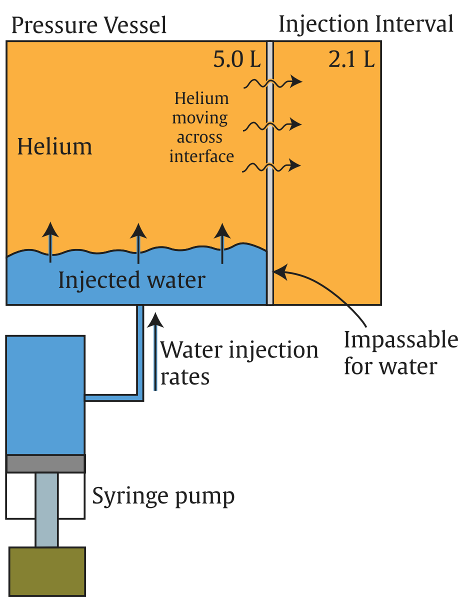

Fig. 10. Tank model to convert injection rates of water into the pressure vessel to helium rates leaving the vessel.

4. Results

Three different simulations were carried out to explore the effects of coupling and permeability modifications. The first simulation is a TOUGH3-only simulation, without mechanical coupling or permeability changes, restricting the model to the two-phase flow gas transport mechanism. This simulation focuses on understanding how much gas must enter the Opalinus Clay to reproduce the pressure evolution prior to the observed pressure drop at 4.2 MPa. Additionally, it provides insight into the pressure reduction caused by visco-capillary gas entry, helping to evaluate the extent to which two-phase flow processes alone can explain the observed pressure behavior.

The second and third simulations build on the same TOUGH3 setup used in the first simulation, but incorporate mechanisms to account for permeability increases due to the onset of dilatancy-controlled gas flow. In the second simulation, permeability is modified using a gas pressure-based approach, where it increases once a threshold pressure is exceeded. In the third simulation, TOUGH3 is coupled with FLAC3D,

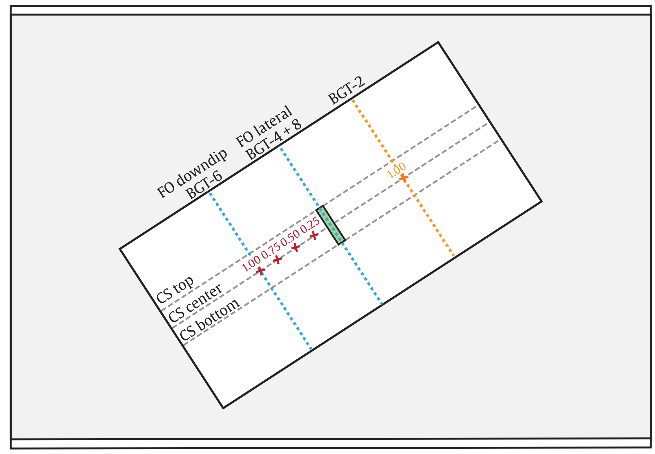

Fig. 11. Evaluation locations in model. Red and orange crosses: points at which pressure and saturation are evaluated. Dashed gray lines: locations of cross-sections used to assess permeability evolution. Blue dashed line: location of the section along which deformation is evaluated in that orientation, corresponding to the placement of FO cables installed during the experiment. Orange dashed line: location of BGT-2. (For interpretation of the references to color in this figure legend, the reader is referred to the web version of this article.)

allowing elastic and plastic strain values computed in FLAC3D to modify the permeability field. This enables investigation of how mechanical deformation influences gas migration through the clay.

For each simulation, we evaluated the modeled pressure within the injection interval, as well as at four points down dip (red crosses in Fig. 11) and one point up dip (orange cross in Fig. 11) from the injection zone. The points furthest from the injection interval correspond to the locations of the observation boreholes. The evaluated up-dip pressure point corresponds to one interval in the pore pressure observation borehole (BGT-2), which is the only borehole from which pore pressure data were recorded during the experiment. In the two simulations where permeability is modified, we additionally present three cross-sections showing the spatial evolution of the enhanced permeability (dashed gray lines in Fig. 11). For the strain-based permeability simulation, we compute the modeled strain in the direction of the FO cables at their installed locations (blue lines in Fig. 11, corresponding roughly to boreholes BGT-4, BGT-6 and BGT-8), to enable qualitative comparison with the observed strain measurements. The FO cable in BGT-2, located up-dip from the injection interval, was not mounted directly to the rock but was installed in water and clamped to the packers. As a result, the recorded signal does not fully represent rock deformation, and BGT-2 was therefore only used for comparison of pore pressure evolution.

4.1. Baseline two-phase flow simulation

The results from the two-phase flow simulation using TOUGH3 are shown in Fig. 12. After correcting the helium injection rates and accounting for the tank refill events, the model provides a good match to the pressure evolution leading up to the observed pressure drop at 4.2 MPa. However, the sharp pressure drop from 4.2 to 3.2 MPa is not captured in the model. Instead, the simulated pressure continues to rise, reaching values as high as 7.5 MPa by the end of the simulation, whereas the measured pressure levels off at approximately 3.3 MPa.

The hydraulic and van Genuchten parameters were adopted from NAGRA[17] and are listed in Table 1. Using the parameter set described in Section 3.1, the model reproduces the observed injection pressure evolution prior to the pressure drop at 4.2 MPa (orange line in Fig. 12). In the adopted TOUGH3 formulation, this required an apparent gas entry pressure of 60 MPa, compared to the value of 34 MPa reported by NAGRA.[17]

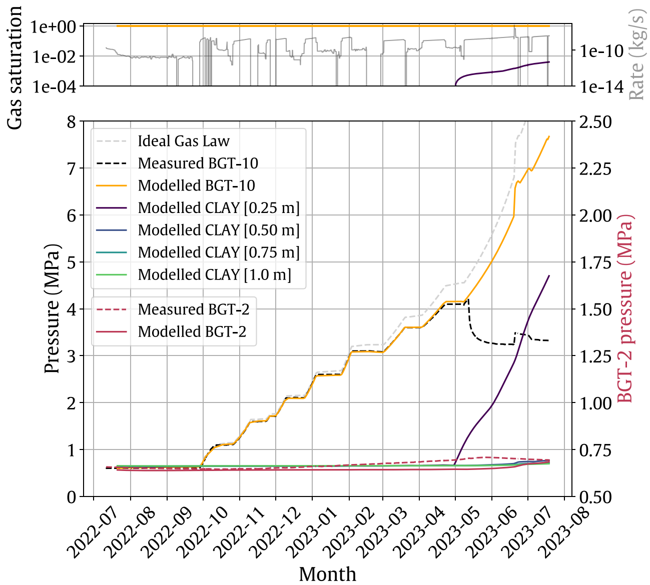

Fig. 12. Gas saturation and helium injection rates (top) and gas pressure (bottom) evolution for one element in the injection interval (orange) and five surrounding elements at varying distances from the injection interval (see Fig. 11). Results are from the TOUGH3-only simulation without permeability modification. The modeled and measured pressure in the interval of the observation borehole (purple-red color) is plotted on the secondary *y*-axis (bottom). (For interpretation of the references to color in this figure legend, the reader is referred to the web version of this article.)

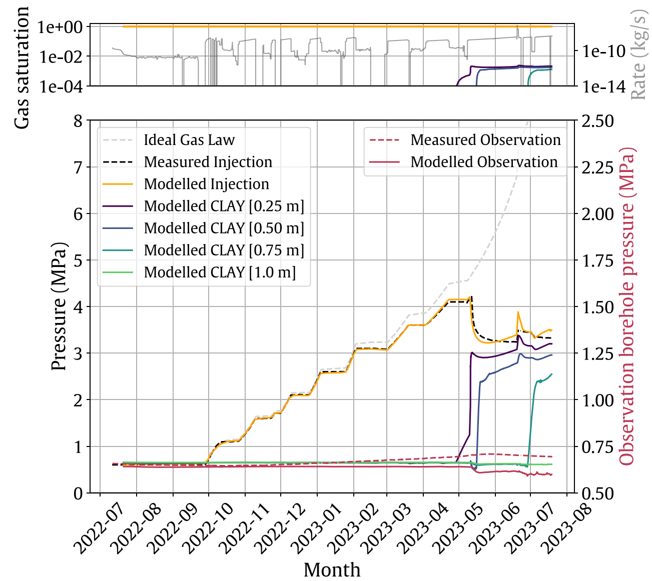

Fig. 13. Gas saturation and helium injection rates (top) and gas pressure (bottom) evolution for one element in the injection interval (orange) and five surrounding elements at varying distances from the injection interval (see Fig. 11). Results are from the simulation with gas pressure based permeability modification. The modeled and measured pressure in the interval of the observation borehole (purple-red color) is plotted on the secondary *y*-axis (bottom). (For interpretation of the references to color in this figure legend, the reader is referred to the web version of this article.)

As can be seen from the saturation and pressure response of the clay element located 0.25 m from the injection interval (purple line in Fig. 12), gas entry into the surrounding clay remains confined within a distance of approximately 0.25 m until shortly before the peak pressure in the injection interval is reached, after which the pressure in this clay element begins to increase rapidly upon gas entry. In contrast, the modeled pressures at the evaluated points located 0.5, 0.75 and 1.0 m from the injection interval remain relatively stable. The pressure recorded in BGT-2, marked by the dashed purple-red line in Fig. 12 and corresponding to the secondary *y*-axis on the right, increases from approximately 0.65 MPa to a peak of 0.71 MPa on 26 May 2023. This peak occurs approximately 14 days after the measured BGT-10 pressure peak. In contrast, the modeled BGT-2 pressure remains relatively stable throughout this period and is approximately 0.65 MPa at the time the measured BGT-2 pressure reaches its peak. Following the peak, the measured BGT-2 pressure gradually decreases to approximately 0.69 MPa by the end of the simulation period. In contrast, the modeled BGT-2 pressure continues to increase from approximately 0.65 MPa to 0.68 MPa, following the continued increase in the modeled pressure within BGT-10.

For reference, the figure also includes the pressure curve calculated using the ideal gas law, which represents the theoretical case in which no gas escapes from the injection interval. This curve is shown as a dashed light gray line in Fig. 12. Just prior to the observed pressure drop, the ideal gas law predicts a pressure of approximately 4.7 MPa, which is about 0.5 MPa higher than the observed pressure of 4.2 MPa.

4.2. Dilatancy-induced permeability increase: Gas pressure based approach

Results from the gas pressure–dependent permeability model are shown in Fig. 13. A good agreement between the modeled and measured pressure evolution in the injection interval was achieved using the hydraulic parameters listed in Table 1 and the pressure–permeability relationships defined in Eqs. (18) and (19) combined with the empirical constants given in Table 4. Modeled pressures remained within a range of 0.12 MPa of the measured values throughout the pressure drop phase.

Compared to the uncoupled simulation (Fig. 12), the gas pressure and saturation in the gas pressure-based model propagate significantly further into the formation. In the uncoupled case, the pressure front reaches only the first evaluation point at 0.25 m down-dip (purple line in Fig. 12), whereas in the gas pressure-based model, it reaches up to 0.75 m (blue line in Fig. 13) at the end of the simulation.

The pressure response in the observation borehole remains steady at approximately 0.64 MPa up until the onset of the pressure drop, at which point it quickly decreases to 0.61 MPa, and then gradually stabilizes at 0.60 MPa. Similar to the uncoupled simulation, the modeled pressure response therefore does not reproduce the gradual pressure increase observed in BGT-2 prior to the pressure drop.

The spatial evolution of permeability enhancement is shown in Fig. 14, which contains cross-sections through the top, center, and bottom of the model domain (see Fig. 11) at two time steps: 8 and 61 days after the pressure peak of 4.2 MPa. At 8 days post-peak, the area of enhanced permeability has a diameter of approximately 0.75 m at the top and bottom, and 1.0 m at the center. The maximum permeability at this stage reaches 7.1×10^{-18} m^2. By 61 days post-peak, the permeability enhancement has expanded further to a diameter of approximately 1.4 m (top and bottom) and 1.6 m (center), and a maximum permeability of 8.5×10^{-18} m^2.

At both evaluated time steps, the permeability within the disturbed zone remains nearly uniform and radially symmetric, with values consistently within the same order of magnitude. Between 8 and 61 days after the pressure peak, the permeability increases only modestly by approximately 20%. The most significant change between these two time steps is the spatial extent of the disturbed zone, rather than the magnitude of permeability enhancement itself.

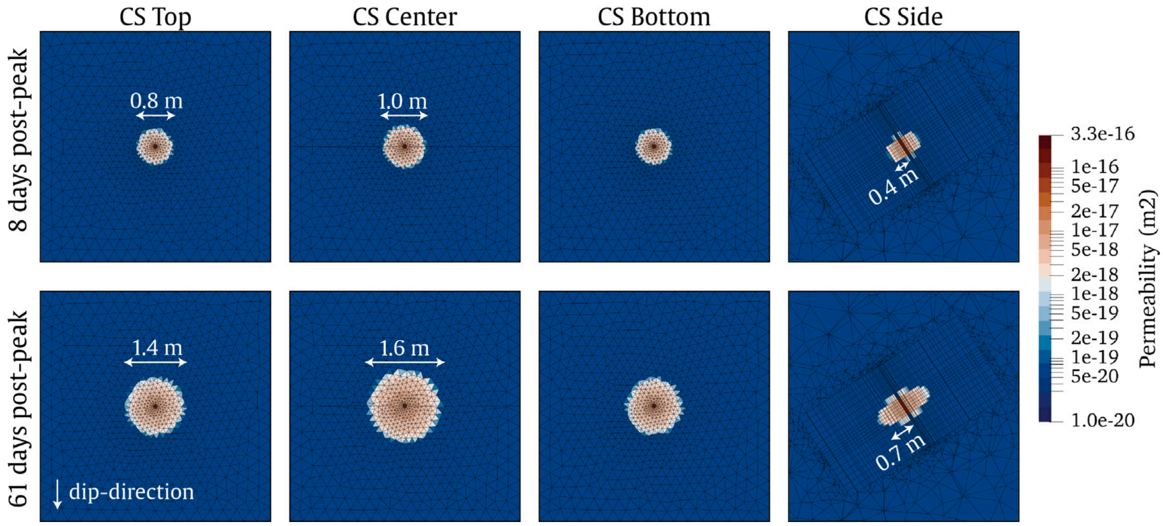

Fig. 14. Permeability evolution in the model domain at two different times following the peak injection pressure of 4.2 MPa, shown for four different cross-sections through the model (see Fig. 11), using the gas pressure based permeability model.

4.3. Dilatancy-induced permeability increase: Strain based approach

4.3.1. Pressure response and permeability calibration

The results from the strain-based permeability approach are presented in Fig. 15. A good match between the observed and modeled pressure evolution was achieved using the hydraulic parameters listed in Table 1, the mechanical parameters from Table 2, the applied stress conditions in Table 3, and the empirical permeability modifiers summarized in Table 4. Similar to the gas pressure-based approach, the gas saturation and pressure fronts advance farther in this model than in the uncoupled simulation. Rapid increases in pressure at the observation points located 0.25 m and 0.5 m down-dip from the injection interval occur at similar times in both permeability approaches. However, the front only reaches the evaluation point at 0.75 m down-dip near the end of the simulation, approximately 19 days later than in the gas pressure-based model, as shown in the gas saturation plot.

The modeled pressure at the observation borehole remains stable at approximately 0.64 MPa until mid-May 2023, after which it gradually decreases and stabilizes around 0.60 MPa over the course of a month. Similar to the gas pressure-based approach, this trend does not match the observed pressure evolution in BGT-2. Unlike the gas pressure-based approach, the strain-based model shows a rapid increase in modeled pressure near the end of the simulation, coinciding with gas entry into the observation element.

Peak and residual bedding-plane friction angles (φ_j, φ_{jr}) and the empirical constants governing permeability evolution (k_f, b_1, b_2) were treated as calibration parameters. Due to poro-elastic coupling and associated shear-stress changes (including stress redistribution under strain softening), the best-fitting bedding-plane friction angles were found to be 17.3° (peak) and 13.8° (residual), which reproduce failure at the observed peak pressure.

Fig. 16 shows the stress evolution in a clay element adjacent to the injection interval. As pore pressure increases through time, the effective normal stress decreases while the shear stress remains relatively stable. At an effective normal stress of approximately 3.8 MPa, a sudden increase in shear stress is observed, indicating that a nearby element has failed and caused local stress redistribution. This element then fails shortly after, and its stress state transitions to the residual strength envelope.

Following the mechanical calibration, we adjusted the parameters governing permeability enhancement. In the initial implementation, permeability evolved continuously based on Eq. (20), meaning that the initial permeability k_{ini} in this equation remained unchanged even

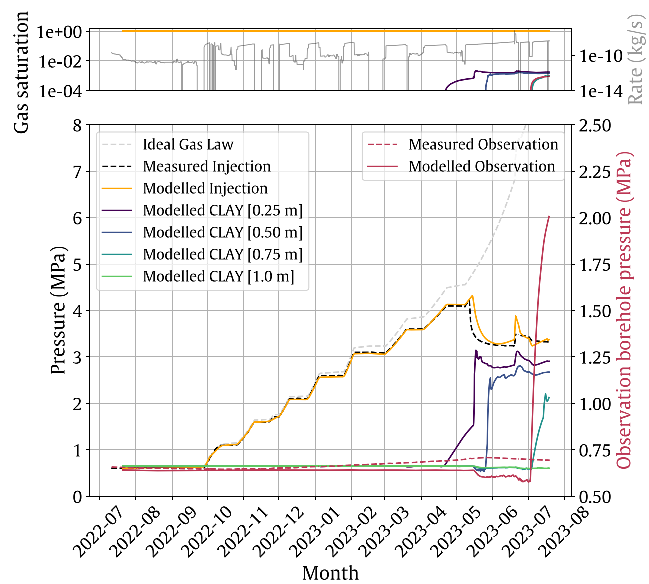

Fig. 15. Gas saturation and helium injection rates (top) and gas pressure (bottom) evolution for one element in the injection interval (orange) and five surrounding elements at varying distances from the injection interval (see Fig. 11). Results are from the simulation with elastic/plastic strain based permeability modification. The modeled and measured pressure in the interval of the observation borehole (purple-red color) is plotted on the secondary *y*-axis (bottom). (For interpretation of the references to color in this figure legend, the reader is referred to the web version of this article.)

after plastic strain initiation and was not updated to a distinct failure permeability k_f once the plastic strain exceeded zero. However, this approach did not reproduce the rapid pressure drop observed in the data. We could recreate the rapid pressure drop by setting the b_2 constant to a much higher value, thereby amplifying the permeability increase in response to plastic strain. This led to some permeability values to be 4–5 orders of magnitude higher than the initial value. As a consequence, the pressure in the injection interval did not stabilize after the initial drop, but instead continued to decrease. We therefore introduced a failure permeability parameter k_f in Eq. (21): once an element fails, its permeability is increased from the initial value to the specified failure permeability, which in this case is 100 times the initial

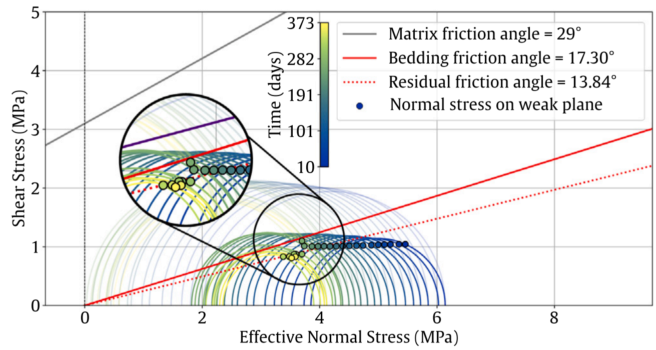

Fig. 16. Stress evolution in a clay element adjacent to the injection interval.

permeability. Further enhancement of permeability is then governed by the accumulated elastic and plastic strains. The final set of parameters used is listed in Table 4.

The permeability evolution for three cross-sections (see Fig. 11) and a vertical slice through the center of the model is shown in Fig. 17 for two time steps: 8 and 61 days after the pressure peak of 4.2 MPa. At 8 days post-peak, a directional preference in permeability development becomes apparent: in the upper region (CS Top), the area of enhanced permeability tends to propagate up-dip, while in the lower region (CS Bottom) it evolves in the down-dip direction. This directional pattern remains visible at 61 days post-peak, though less pronounced. Over this time interval, the zone of permeability enhancement expands from approximately 0.7 to 1.3 m in extent in CS Top, and from approximately 1.0 to 1.4 m in CS Bottom. Peak permeability values between 8 and 61 days post-peak increase by only about 3%, with values of around $6–7 \times 10^{-18}$ m^2 found in the regions of enhanced permeability.

To evaluate the influence of the permeability evolution constant b_2, we performed a brief sensitivity analysis by varying its baseline value by ±10%. Fig. 18 shows the corresponding pressure curves as well as the calculated dimensionless sensitivities. The analysis indicates that b_2 only becomes influential once the pressure drop occurs, after which the sensitivity reaches values up to 0.6. In practical terms, this means that a 1% increase in b_2 leads to an approximately 0.6% change in interval pressure during this stage of the simulation.

4.3.2. Strain response

Strain evolution along the axis of four boreholes was modeled (see Fig. 11) and compared with FO strain measurements.[13] Strain changes were evaluated between one day prior to the observed pressure peak and 5 and 35 days afterwards (Fig. 19). In each subplot, the dashed black line marks the equivalent injection interval depth, defined as the interval between CS Top and CS Bottom at the location of each evaluated borehole (see Fig. 11).

The measured data reveal distinct strain responses across the boreholes. BGT-4 exhibits localized extension (positive) and compaction (negative) in the range of 5–15 με both 5 and 35 days after the pressure drop, with a stronger compaction signal near the injection interval depth becoming more prominent 35 days after. BGT-8 shows a more pronounced extensional signal of up to 20 με centered on the injection interval depth, which slightly decreases 30 days later, whereas the compaction signal in this time period increases. The most prominent response is seen in BGT-6, where a strong extension signal develops around a depth of 14.4 m, slightly below the equivalent injection interval, with values reaching up to 70 με.

Comparing the modeled strain to the measurements, we find that after 5 days the simulated strain changes remain minimal across all boreholes. By 35 days, however, the simulated extension increases and reaches the same order of magnitude as the observed values. In particular, a comparable magnitude of extensional strain is reproduced in BGT-8 and BGT-6 at the injection interval depth. In BGT-4 and BGT-8, the model predicts extension of up to 15 με at the equivalent injection interval depth. In BGT-2, the model yields extension of up to 74 με localized near the top of the injection interval. The strongest simulated response occurs in BGT-6, where extension reaches up to 108 με localized near the lower part of the injection zone.

While the simulated extension is broadly comparable to the measured extension, the compressive signal is significantly under-predicted by the model. This discrepancy is most evident in BGT-4, where the measured compaction reaches up to 16 με, whereas the simulated values do not exceed 2 με. The largest simulated compaction is 10 με, occurring beneath the main extension zone in BGT-6.

5. Discussion

This study aimed to improve our understanding of gas transport mechanisms in undisturbed Opalinus Clay by developing coupled hydro-mechanical models. Specifically, we applied permeability models that incorporate the onset of dilatant pathway formation to simulate the GT-experiment at the Mont Terri Rock Laboratory. Our results demonstrate that these models are capable of capturing key features of the observed pressure response and provide insights into the evolution of permeability, while also enabling a better understanding of the timing, occurrence, and relative contribution of distinct gas transport mechanisms throughout the experiment.

5.1. Modeling and occurrence of two-phase flow

To identify which gas transport mechanisms were active during different phases of the experiment, we first conducted a TOUGH3-only simulation that accounted solely for two-phase flow, without mechanical coupling. This simulation showed that two-phase flow alone could not explain the observed pressure drop from 4.2 to 3.2 MPa. By comparing the observed pressures with those estimated using the ideal gas law based on injection rates, we found a discrepancy starting already at approximately 2.5 MPa that indicated helium began entering the clay matrix. We therefore interpret two-phase flow to begin occurring around this pressure and to contribute to the difference between the observed pressure and the ideal gas law calculations.

However, in order to reproduce the observed pressure evolution prior to the pressure drop, the apparent gas entry pressure in the van Genuchten model ($1/\alpha$) had to be increased from the 34 MPa reported by NAGRA[17] to 60 MPa when using the standard TOUGH3 formulation for gas relative permeability. As mentioned in Section 3.1, this adjustment is related to differences in the implementation of gas relative permeability between TOUGH3 and the formulation used by NAGRA.[17] To investigate the influence of this difference, an additional simulation was carried out in which the exponent in Eq. (8) was increased from 1/3 to 1/2 (Supplementary Fig. 1). This modification produces gas relative permeability values that are similar to those used by NAGRA[17] for low gas saturations ($S_g < 0.02$), which is appropriate because the modeled gas saturations remain below 0.01 throughout the simulation. Using this modified formulation, a good agreement between the modeled and measured injection pressures was obtained with an apparent gas entry pressure of 34 MPa, consistent with the value reported by NAGRA.[17] This indicates that the higher apparent gas entry pressure required in the standard TOUGH3 simulations primarily results from differences in the gas relative permeability formulation at low gas saturations.

The presence of two-phase flow in the Opalinus Clay has also been suggested in previous studies. For instance, Marschall et al.[8] proposed that imbibition of gas through the existing pore space may occur through macropores, which represent approximately 10%–30% of the total pore space. However, other authors suggest that the classical two-phase flow approach may not be appropriate for clay-rich rocks due to capillarity restrictions on gas penetration of the inter-granular

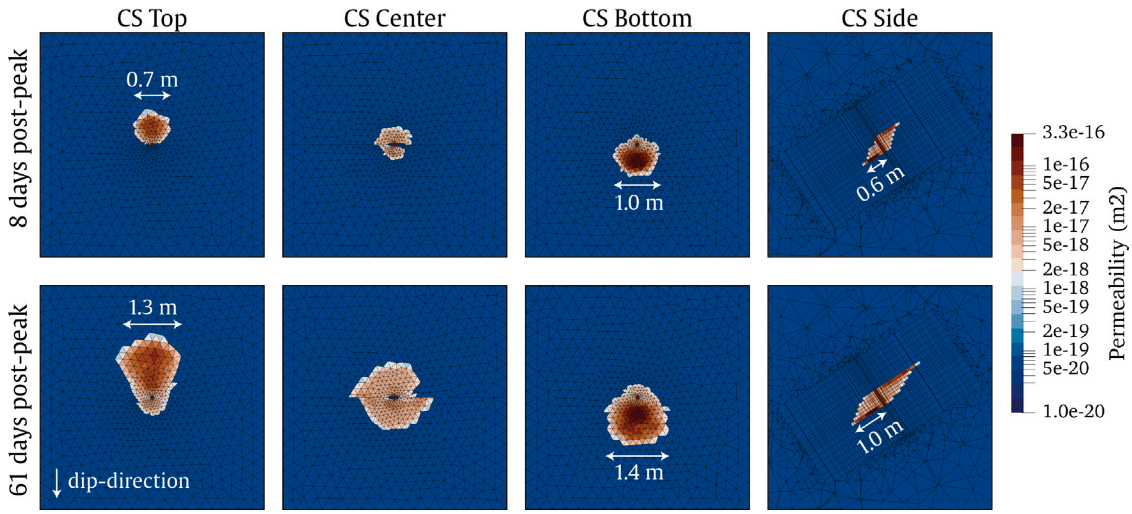

Fig. 17. Permeability evolution in the model domain at two different times following the peak injection pressure of 4.2 MPa, shown for four different cross-sections through the model (see Fig. 11), using the strain based permeability model.

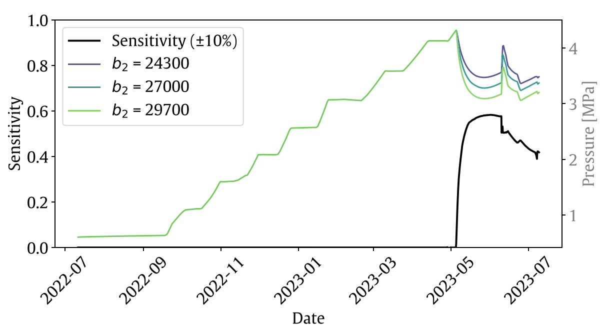

Fig. 18. Sensitivity analysis of empirical parameter b_2 used in Eq. (20).

saturated pores. Laboratory studies on Callovo-Oxfordian claystone by Harrington and Horseman[9] and Cuss et al.[33] suggest that gas flow is restricted by pressure-induced dilatant pathways. Although these findings are based on a different claystone, it shares similar properties with Opalinus Clay, and it is therefore reasonable to consider this in the context of our experiment. An alternative interpretation of the deviation from the ideal gas law prior to breakthrough, which aligns with the gas flow restrictions proposed in these studies, is the early formation of smaller dilatant pathways. Gas begins to enter the formation along these pathways, followed by the gradual development and slow propagation of a dendritic network of gas flow channels, corresponding to stages 1 and 2 in Cuss et al.[33] The pressure drop occurring at the breakthrough event would then result from the sudden formation of a more prominent network of dendritic dilatant pathways that developed along a weaker bedding plane, as described in stage 3 of Cuss et al.[33] The earlier stages preceding the pressure drop could, in this case, be simulated by increasing the parameters a_1 in Eq. (18) and b_1 in Eq. (20), thereby allowing for a gradual increase in permeability associated with the initial development of dilatant pathways. To compensate for this earlier onset of permeability change, an even higher apparent gas entry pressure would be required to prevent premature two-phase flow. However, implementing this level of model refinement was beyond the scope of the present study, as we aimed to keep the phase preceding the pressure drop as simple and constrained as possible.

5.2. Modeling and occurrence of dilatant pathways

5.2.1. Comparison of permeability enhancement approaches

Two different approaches to model the onset of dilatant pathways successfully reproduced the 1 MPa pressure drop, which we interpret as being caused by these pathways. In both cases, the area of enhanced permeability between the two evaluated time steps was of similar size, and the overall enhanced permeability values ranged between 10^{-17} and 10^{-18} m^2 (Figs. 14 and 17). However, the two approaches differ significantly in the way permeability enhancement is represented, resulting in both advantages and limitations that are discussed below.

The gas pressure-based approach reproduced the measured injection pressure evolution reasonably well and provided a first estimate of the permeability enhancement required to simulate the observed pressure drop. However, permeability enhancement in this model is controlled directly by gas pressure rather than by a mechanical parameter, meaning that the effects of a mechanical process are represented without explicitly incorporating the underlying mechanical processes. In addition, the FO strain measurements (Fig. 19) indicate that the deformation response is strongly localized, whereas the gas pressure-based approach produces a comparatively uniform region of enhanced permeability. This relatively uniform permeability field results from the fact that neighboring elements around the injection interval experience similar gas pressures once the permeability-enhancement threshold is reached. Because identical initial permeability and van Genuchten parameters are assigned to these elements, permeability enhancement occurs almost simultaneously and by a similar magnitude throughout the affected region. Although the approach successfully reproduces the observed pressure drop using only a single empirical relationship, it does not capture the localized nature of the inferred dilatant pathways.

We therefore introduced the strain-based approach to better represent the mechanical processes occurring during the development of dilatant pathways. Although incorporating mechanical effects and strain-dependent permeability enhancement introduces additional calibration parameters and degrees of freedom, it provides a more physically based representation of permeability evolution. In addition to reproducing the observed pressure evolution in the injection interval, this approach captures localized permeability enhancement and deformation along bedding planes, showing partial agreement with the localized strain signals observed in the FO measurements. Incorporating pre-existing geological features or heterogeneities, represented

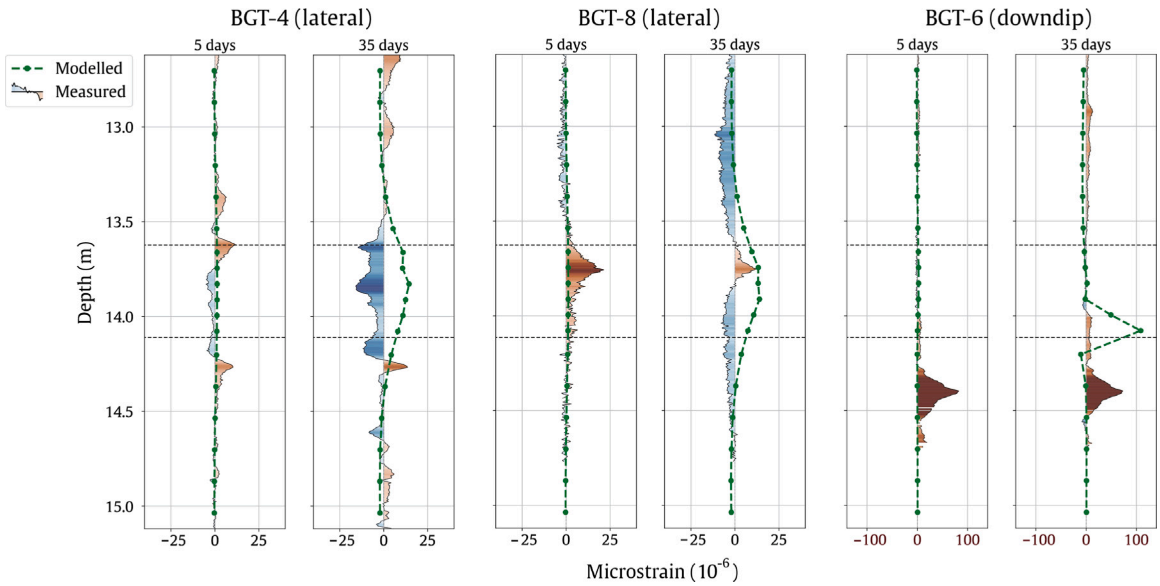

Fig. 19. Measured and modeled strain changes along FO cables in three boreholes (see Fig. 11). Each pair of plots shows the difference in strain between one day before the observed pressure drop (at 4.2 MPa) and 5 days after (left column) or 35 days after (right column), respectively. Positive values (red) indicate extensional strain, while negative values (blue) indicate compressional strain. The green line represents the modeled strain. Dashed black lines indicate the depth corresponding to the injection interval. (For interpretation of the references to color in this figure legend, the reader is referred to the web version of this article.)

as discrete zones with reduced strength and/or enhanced permeability, would likely further improve the reproduction of the observed directionality and degree of localization.

5.2.2. Calibration and sensitivity of the strain-based approach

The variability of permeability values in the strain-based approach arises from the permeability–strain relationship given in Eq. (20) and the choice of empirical constants. Introducing the failure permeability parameter k_f adds an additional degree of freedom, which influences how variations in accumulated plastic strain between failed elements translate into permeability changes. Different combinations of k_f and b_2 can therefore produce a similar pressure drop, provided that the overall permeability enhancement within the disturbed zone remains comparable. For example, testing a combination of $k_f = 5 \times 10^{-18}$ m^2 and $b_2 = 3000$, while maintaining the same anisotropy ratios as in the base case, produced a comparable pressure drop. In this scenario, the average enhanced permeability remained similar to that of the base case, but the permeability values within the disturbed zone became more uniform (around 6–7 $\times 10^{-18}$ m^2). This occurs because the larger value of k_f reduces the relative influence of accumulated plastic strain on the permeability enhancement. The spatial extent of enhancement was similar between the cases, and the directional trends (up-dip propagation at shallower depths, down-dip propagation at greater depths) persisted, albeit less pronounced. There is therefore a broad parameter space in which k_f and b_2 can be traded off to achieve similar pressure responses and transmissivity values along the injection interval, despite small differences in the final spatial distribution of permeability enhancement.

Without the inclusion of k_f, comparable pressure drops can still be reproduced by further increasing b_2. However, in such cases the permeability enhancement becomes entirely controlled by local variations in accumulated plastic strain, resulting in isolated permeability values exceeding 10^{-14} m^2. These values approach permeabilities more commonly associated with gas fracturing rather than dilatant pathway formation in Opalinus Clay. The introduction of k_f therefore serves to limit such unrealistic outliers while still preserving permeability variability associated with the heterogeneous plastic strain field. We chose to present the parameter set given in Table 4, as this combination reproduced the observed deformation patterns and directional trends in permeability development while limiting the occurrence of strong local permeability outliers.

5.2.3. Influence of stress-field assumptions and strain softening on pathway localization

The stress field was simplified by assuming perfectly vertical and horizontal principal stresses, with the intermediate horizontal principal stress aligned with the bedding dip direction (Fig. 6). This represents an idealized stress configuration based on the average orientations reported in previous studies.[22] Although some variability in principal stress orientations has been reported, these deviations are generally small relative to the stress orientation adopted in this study. A rotation of the stress field would slightly modify the normal and shear stresses resolved on the bedding plane and would therefore require small adjustments to the friction angle used to define the onset of dilatant permeability enhancement. In particular, if the vertical principal stress were rotated more toward the bedding dip direction, the resolved shear stress acting on the bedding would increase. Consequently, a higher friction angle would be required in the model to ensure that permeability enhancement through shear failure is initiated at a similar pore pressure increase, thereby maintaining agreement with the timing of the observed pressure drop.

In addition, the model assumes that the ratios between the principal stress remain constant with depth. If these ratios vary with depth, for example if differential stresses increase at greater depth, down-dip failure migration would become more likely because deeper sections along the bedding would be closer to failure. Such a stress gradient could therefore promote preferential propagation of failure in the down-dip direction. However, given the relatively small scale of the modeled domain and experiment (only a few meters), the stress ratios would need to vary substantially over a short distance for this effect to significantly influence the direction of failure propagation.

Another important parameter controlling the evolution and localization of the modeled dilatant pathways in the strain-based approach is the degree of strain softening applied. Strain softening was introduced to better capture the localized deformation observed in the FO strain measurements (Fig. 19). Without strain softening, failure would be more distributed, resulting in slower and delayed permeability enhancement and a correspondingly later pressure drop. The sudden pressure drop and localized strain signatures in the FO data motivated us to introduce softening of the weak-plane strength parameters, either through a reduction in friction angle or a loss of cohesion, thereby promoting strain localization in the model. Because the weak-plane cohesion was assumed to be zero, only the friction angle was allowed to soften.

The softening factor of 0.8 for the bedding-plane friction angle was based on values reported by Winhausen et al.[34] and Ismael et al.[35] on Opalinus Clay. In Ismael et al.,[35] peak and residual cohesion and friction angles for a bi-linear Mohr–Coulomb strength criterion were provided for bedding planes, based on laboratory data from Konietzky et al.,[36] Popp and Salzer,[37] Bock[38] and Thöny.[39] Since we assumed cohesionless rock, we calculated the friction angle required to produce failure under the proposed strength criterion at an effective normal stress of 3.8 MPa, which corresponds to the onset of failure in our simulation (Fig. 7). We performed the same calculation for the residual friction angle and found that the ratio between the peak and residual friction angles was 0.82. In Winhausen et al.,[34] peak and residual differential stresses for a sample with a bedding angle of 37° (close to the GT-experiment bedding angle) under 4 MPa confinement yielded a similar ratio of 0.8 when converted to friction angles assuming zero cohesion. These values correspond to post-failure weakening of fully developed shear planes in laboratory samples rather than to softening behavior directly associated with the initiation and propagation of dilatant pathways. Since the current model represents the onset of dilatant pathway formation and the associated permeability enhancement through shear failure along bedding planes, we assumed that the weakening behavior reported for post-failure shear planes can be used as a first-order approximation for the initiation and propagation of dilatant pathways. In addition, friction-angle softening promotes stress redistribution following bedding-plane failure, allowing more rapid propagation of the shear-failed zone, which within the framework of the present model represents a more rapid propagation of the permeability-enhanced zone and therefore of dilatant pathway development.

The influence of this assumption was evaluated through additional simulations using different softening factors (Supplementary Fig. 2). A simulation without any softening showed that the enhanced permeability field developed more slowly, the pressure drop was smaller, and it occurred later. This delay is attributed to the fact that the first elements to fail were not directly adjacent to the injection interval. Without strain softening, these initial failures transmitted less stress to surrounding cells, delaying their subsequent failure. In contrast, reducing the friction angle by a factor of 0.7 led to slightly earlier failure than observed and, when keeping the mechanical parameters and empirical constants the same as in Tables 2 and 4, resulted in a significantly larger pressure drop. This occurred because the plastic strain values in this simulation were approximately twice as large as those obtained with a friction angle reduction of 0.8. Consequently, the modeled strain along the FO-cables was also approximately twice as large, resulting in a significantly larger deviation from the measured deformation response (Fig. 19). This further supports the choice for a softening factor of 0.8 as a reasonable first-order approximation for reproducing both the pressure response and the observed deformation magnitudes.

5.2.4. Comparison with fiber-optic strain observations

The strain-based approach reproduced several key characteristics of the FO strain response observed during the in-situ experiment. In both the model and the measurements, the strongest extension signal was observed in the down-dip borehole relative to the injection interval (Fig. 19). In particular, the modeled strain difference between one day prior to and 35 days after the pressure drop in BGT-6 reached 108 με, compared to 72 με in the measurements, indicating that the simulated and observed deformation magnitudes are of a similar order. In both cases, the strongest strain response was observed at greater depths within the borehole.

Despite these similarities, important differences remain between the modeled and observed strain evolution. The localized strain signal observed in BGT-6 occurs slightly deeper in the measurements than predicted by the model, relative to the projected position of the injection interval along bedding. This discrepancy may indicate that the bedding dip at depth is steeper than assumed in the model geometry. In addition, strong strain signals are already present in the FO measurements within approximately five days after the pressure drop, whereas in the simulations the deformation develops more gradually and only becomes pronounced after approximately 25 days.

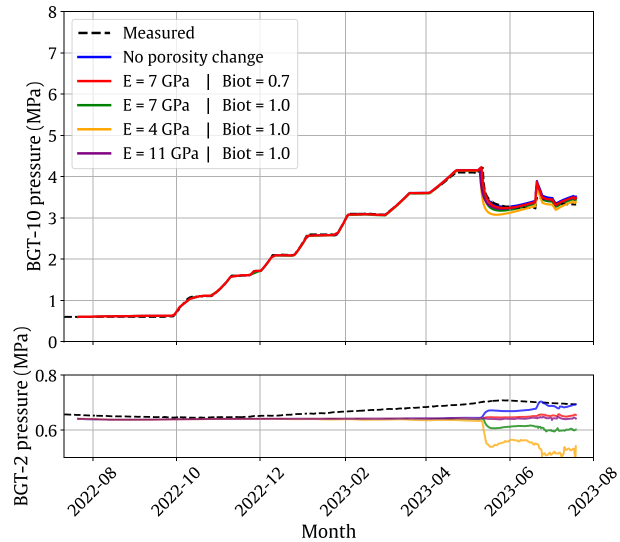

Fig. 20. Gas pressure evolution in the injection interval (top) and at observation borehole BGT-2 (bottom) for the gas pressure-based permeability enhancement approach. Results are shown for the base-case simulation, simulations with modified Young's modulus (4 and 11 GPa), a reduced Biot coefficient (0.7), and a simulation in which poro-elastically induced porosity changes were disabled.

These differences suggest that dilatant pathway formation in the experiment was likely influenced by geological heterogeneity not represented in the current model. The measured FO strain response indicates that deformation initiated preferentially in the down-dip direction, potentially controlled by pre-existing weaknesses and/or a slightly larger-than-hydrostatic pore-pressure gradient at depth, which would reduce effective stress at greater depths and thereby promote down-dip failure propagation. Incorporating such heterogeneities explicitly into the model, for example as discrete zones with reduced strength or enhanced permeability, would likely improve the reproduction of the observed localization and directionality of deformation. Additional refinements, such as imposing a larger pore-pressure gradient and adjusting the assumed bedding dip, may further improve agreement with the FO strain observations.

5.2.5. Pressure response at observation borehole BGT-2

In both coupled models, the modeled pressure at BGT-2 shows a sudden decrease of approximately 0.04 MPa coinciding with the pressure drop in the injection interval, whereas the measured pressure gradually increases by approximately 0.06 MPa during the pressurization phase (Figs. 13 and 15). To investigate whether poro-elastic effects could explain this discrepancy, four additional simulations were performed using the gas pressure-based permeability approach. These included simulations with a lower Young's modulus (4 GPa), a higher Young's modulus (11 GPa), a reduced Biot coefficient (0.7), and a simulation in which poro-elastic porosity changes were disabled entirely (Fig. 20).

The simulation with a lower Young's modulus, corresponding to stronger poro-elastic coupling, resulted in an even larger pressure decrease at BGT-2. In contrast, increasing the Young's modulus or reducing the Biot coefficient produced a more stable pressure response.

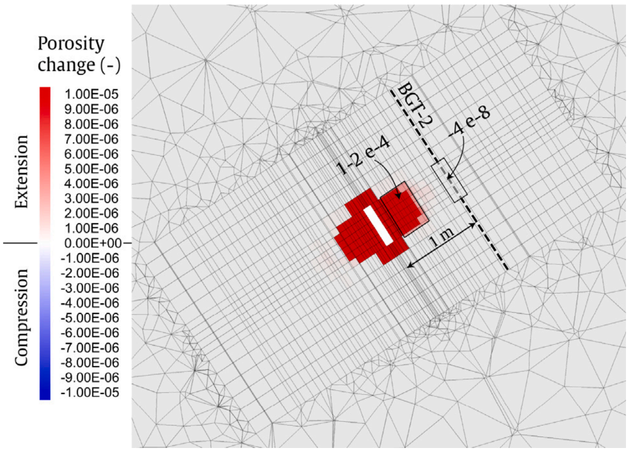

Fig. 21. Cross-section of porosity change relative to the start of the simulation for the gas pressure-based permeability enhancement approach. Red colors indicate porosity increase associated with extension, whereas blue colors indicate porosity decrease associated with compression.

When porosity changes were disabled, the pressure decrease disappeared and a small pressure increase was observed instead. These results indicate that the modeled pressure drop is primarily controlled by porosity changes associated with permeability enhancement.

This interpretation is supported by the porosity evolution of the base-case simulation (Fig. 21). Shortly after the pressure drop, porosity within the permeability-enhanced zone has increased by approximately $1–2\times10^{-4}$, whereas the porosity reduction associated with compression around BGT-2 is only about 4×10^{-8}. As the permeability-enhanced zone propagates toward BGT-2, its substantially larger porosity increase creates a local pressure sink due to the associated reduction in pore-water pressure, which dominates over the small pressure increase associated with compression around the observation borehole. Reducing the poro-elastic response decreases the magnitude of this porosity increase and consequently reduces the modeled pressure drop at BGT-2.

These model results suggest that an area of enhanced permeability did not propagate toward BGT-2 to the extent predicted in the simulations, but instead remained preferentially oriented in the down-dip direction, consistent with the FO strain observations (Fig. 19). At the same time, the discrepancy does not necessarily imply that poro-elastic coupling is overestimated in the model. Further reducing poro-elastic effects by increasing the Young's modulus or lowering the Biot coefficient would also reduce the modeled deformation response, whereas the strain signal in boreholes such as BGT-6 already arrives later in the simulations than observed experimentally.

A plausible explanation for the observed pressure increase at BGT-2 is that geological heterogeneity, which is not represented in the current model, influenced the direction of pathway development. Such a feature could promote a more localized propagation of the permeability-enhanced zone in the down-dip direction. As fluid flow would be concentrated within a smaller region, the permeability-enhanced zone would experience stronger extension and therefore a larger local porosity increase. At the same time, this would concentrate the dilatant response farther away from BGT-2, preventing the formation of the local pressure sink near the observation borehole. The stronger localized extension could also induce a larger compressive response in the surrounding rock mass, including in the direction of BGT-2. Under such conditions, BGT-2 would experience the poro-elastic pressure increase associated with compression while remaining sufficiently distant from the permeability-enhanced zone to avoid the pressure reduction caused by the nearby porosity increase. This mechanism would be more consistent with the observed gradual pressure increase at BGT-2 while preserving the overall deformation response indicated by the FO measurements.

5.2.6. Influence of gas injection rate on pathway development

To investigate the influence of gas injection rate on dilatant pathway development, additional simulations were performed using the strain-based approach and injection rates corresponding to 0.5, 1 and 10 times the average gas injection rate applied during the GT-experiment. The results are shown in Fig. 22.

The simulations indicate a relationship between gas injection rate, the pressure at which permeability enhancement is initiated, and the resulting pressure-drop magnitude. Higher injection rates lead to permeability enhancement at lower pressures and produce larger permeability increases within the enhanced zone, while the associated pressure drops become smaller. This occurs because the continued gas supply partly compensates for pressure dissipation associated with gas migration away from the injection interval. The earlier onset of permeability enhancement reflects the reduced time available for stress redistribution around the injection interval during more rapid pressurization.

In contrast, lower injection rates show a stronger influence of two-phase flow prior to permeability enhancement. This is evident from the deviation from the initially linear pressure increase before the pressure drop, particularly for the simulation with an injection rate of 0.5 times the GT average. Under these conditions, gas progressively migrates into the surrounding clay before permeability enhancement occurs, resulting in a larger pressure drop once a connected permeability-enhanced zone develops.

The simulations also show that higher injection rates promote a more extensive permeability-enhanced region. The maximum extent of permeability enhancement at the end of the simulation increased from approximately 1.13 m for the lower injection rate (Supplementary Fig. 3) to 1.47 m for the 10-times-higher injection rate (Supplementary Fig. 4). In addition, permeability values in the enhanced zone increased more rapidly and reached the imposed upper limit of 10^{-15} m^2 in the high-rate simulations.

These observations have implications for gas migration in deep geological repositories. Gas generation rates associated with corrosion and degradation processes are expected to be substantially lower than the injection rates applied during the GT-experiment. Under such conditions, a larger fraction of the generated gas would likely dissipate through two-phase flow before permeability enhancement occurs. The resulting permeability-enhanced zone would therefore be expected to remain smaller and exhibit lower permeability values than those observed in the present simulations. Although the onset of dilatant pathways may still result in a pronounced pressure drop, the disturbed volume of host rock would likely be more limited because of the lower gas generation rates and slower pathway propagation.

5.2.7. Implications for dilatant versus tensile failure

Lastly, the question remains whether the same pressure signal could be reproduced using a tensile gas-fracture mechanism, even though this appears unlikely based on the interpretation of the first gas-entry event by Cuss et al..[13] Their interpretation is based on both the observed pressure evolution and the FO strain response. In particular, the progressive dilatant pathways is more likely attributed to the relatively slow pressure decay toward a stable value (over ~37 days), the relatively high pressure asymptote after the pressure drop, and the delayed development of the maximum FO strain signal (on the order of ~36 h). All these are against a rapid tensile fracture propagation. In contrast, they suggest that the second gas-entry event (Fig. 4) is more indicative of a fracture or bedding-plane split, as it exhibits a larger pressure drop, a faster decay, and a much more rapid strain response.

Focusing on the modeling implications, reproducing the first gas-entry event using tensile failure would pose several challenges. First, the initial normal stress acting on bedding planes is nearly 6 MPa, so tensile opening along bedding is unlikely even without considering any tensile strength. Tensile failure would therefore be expected to occur closer to the orientation of the minimum principal stress rather than along bedding, which appears inconsistent with the FO observations

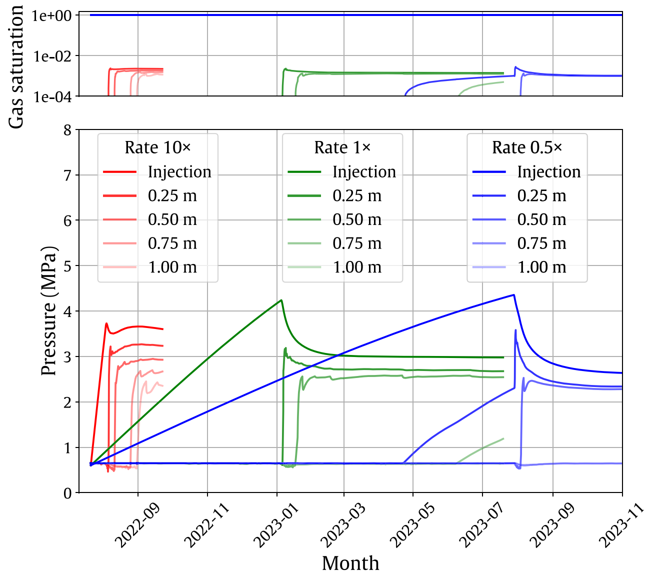

Fig. 22. Gas saturation (top) and gas pressure (bottom) evolution in the injection interval and at four elements located at increasing distances down-dip from the injection interval (see Fig. 11). Results are shown for simulations with fixed helium injection rates corresponding to 10× the average injection rate (red), 1× the average injection rate (green), and 0.5× the average injection rate (blue). Within each color group, progressively lighter shades indicate increasing distance from the injection interval. (For interpretation of the references to color in this figure legend, the reader is referred to the web version of this article.)

indicating that the dominant extensional response is aligned with the bedding-dip direction. Second, while the minimum principal stress in our model is 2.9 MPa, tensile failure requires that pore pressure exceeds the minimum principal stress plus the tensile strength. Reported tensile strengths for Opalinus Clay are on the order of 1–2 MPa[40], with values around 1 MPa reported for orientations perpendicular to bedding; for orientations that do not align with bedding, the effective tensile strength is thus likely higher. Even when adopting the lower bound of 1 MPa, tensile opening would require pore pressure increase exceeding ~3.9 MPa, whereas the pore-pressure increase prior to the main pressure drop is ~3.6 MPa. Finally, even if tensile failure could be triggered, it would likely produce a highly conductive feature with a stronger local pressure gradient, which would tend to localize the response and limit far-field propagation compared to the progressive, shear-driven dilation mechanism represented in our simulations.

5.3. Implications and comparison with previous work

Both Marschall et al.[8] and Jockwer and Wieczorek[7] conducted nitrogen injection tests in the Opalinus Clay at the Mont Terri Rock Laboratory, about 4 m shallower than the GT-experiment. In both studies, characteristic pressure drops in the measurements were interpreted as being caused by the onset of dilatant pathways. In Marschall et al.,[8] gas was injected in a borehole drilled perpendicular to bedding in a step-wise pressure increase, raising the interval pressure to 2.78 MPa, after which it decayed to 2.42 MPa over a period of 30 days. An extensometer located 0.8 m from the injection borehole recorded an extension of approximately 30 με during this period. In the same study, Marschall et al.[8] also conducted a hydrofracture test, which only succeeded at about 9 MPa and resulted in a transmissivity increase of five orders of magnitude. In contrast to the step-wise pressure increases in Marschall et al.,[8] Jockwer and Wieczorek[7] conducted constant-head tests in boreholes drilled both parallel and perpendicular to bedding. Gas entry pressures of 2.0–3.4 MPa were interpreted as the onset of dilatant pathways, followed by pressure drops of 1.5–2.0 MPa within ~2 days and slower stabilization over ~14 days. Repeat injections yielded lower entry pressures, suggesting that the original conditions of the clay had not fully recovered, even up to 140 days after the first gas entry.

Our results are most comparable to Jockwer and Wieczorek,[7] which also reported a rapid pressure drop under constant-head injection. The additional simulations presented in Section 5.2.6 indicate that continued gas injection promotes the further propagation of dilatant pathways and enlargement of the permeability-enhanced zone. This suggests that maintaining gas supply during gas entry allows the pathway network to continue developing, resulting in a more extensive disturbed region around the injection interval.

In contrast, in Marschall et al.,[8] gas injection was stopped once the target pressure was reached. The absence of continued gas supply may have limited the further development and propagation of dilatant pathways, resulting in a smaller permeability-enhanced zone. Consequently, gas migration may have occurred through a less developed dendritic pathway network, potentially corresponding to stage 1 or stage 2 of the pathway evolution framework proposed by Cuss et al.[33] and discussed in Section 5.1, rather than the more extensively connected pathway network inferred for the GT-experiment.

The same difference is evident when comparing strain signals. Averaging our FO strain over 14.2–14.6 m yields 30 με, similar to the extensometer measurements reported by Marschall et al.,[8] but our signal developed within hours rather than 30 days. We attribute this faster response to the same mechanism: continued gas injection during gas entry likely promoted more rapid propagation of dilatant pathways and the associated stress redistribution around the injection interval.

Our onset pressure (4.2 MPa) remains well below the 9 MPa needed for hydrofracture in Marschall et al.,[8] and our simulated transmissivity increase (~2 orders of magnitude) is far smaller than the 5 orders for hydrofracture. The lower entry pressures observed in repeat injections of Jockwer and Wieczorek[7] are consistent with our second gas breakthrough at ~3.7 MPa after three months. In both cases, the reduced onset pressure indicates that once dilatant pathways have formed, the clay does not fully return to its original state within several months. This persistence of slightly weakened conditions is in line with the interpretation of dilatancy-controlled pathway formation rather than discrete hydrofracturing. Overall, the close agreement in onset pressures, pressure drops, strain magnitudes, and transmissivity increases supports our interpretation of the GT-experiment as being dominated by dilatant pathway formation.

A third relevant study is the HG-B gas injection experiment at Mont Terri, described and modeled by Xu et al..[30] Stepwise nitrogen injection produced small pressure decreases once pressures exceeded 1.2 MPa, followed by a larger drop from 2.2 to 0.75 MPa when dilatant pathways connected to a nearby seismic borehole acting as a sink. Xu et al.[30] applied both gas pressure and strain-based permeability enhancement approaches to simulate the onset of dilatant pathways and the associated pressure signals. The gas pressure method reproduced the pressure drops up to the sink connection, with permeability increases of about two orders of magnitude and preferential flow along bedding due to permeability anisotropy, consistent with our findings. In contrast, the strain-based approach linked permeability to Mohr–Coulomb failure of the clay matrix rather than bedding failure as in our study. Their assumed stress state (σ_3 = 0.8 MPa, σ_1 = 7 MPa) imposed much larger differential stresses than ours, leading to matrix failure already at a gas pressure of 1.2 MPa. This approach also yielded more variable permeability, with localized increases of up to three orders of magnitude depending on the failure pattern. Overall, despite differences in threshold pressures, stress assumptions, failure criterion, and test geometry, both studies demonstrate permeability enhancements of two to three orders of magnitude and pressure responses comparable to our observations and modeling, supporting a consistent interpretation of dilatant pathway formation.

In the compared studies, only Xu et al.[30] explicitly modeled the interpreted dilatant pathways using permeability models. A broader comparison of enhanced permeability models in clays is presented by Radeisen,[41] who shows that the elastic contribution to permeability evolution is generally either formulated directly as a function of volumetric strain, or introduced indirectly through porosity updates that are themselves controlled by volumetric strain. For instance, the approach applied by Xu et al.[30] treats the elastic contribution to permeability in a manner similar to the model proposed by Rutqvist et al.,[42] and yields comparable trends to the formulation of Olivella and Alonso.[43] In addition, Zhu and Wei[44] developed a modeling framework for microcrack evolution in coal in which the elastic permeability response differs, but the permeability enhancement associated with microcrack development follows the same general concept as how Xu et al.[30] models the onset of dilatant pathways. In both approaches, permeability is rapidly increased using an exponential dependence on a damage-related variable. Taken together, these comparisons indicate that broadly similar formulations are used to represent the elastic contribution and show a comparable modeling approach for capturing the more rapid permeability enhancement associated with dilatant pathway formation, namely linking permeability changes to the accumulation of inelastic deformation. In this context, we consider the approach of Xu et al.[30] to be well suited for the GT-experiment, as it shares the same general formulation for the elastic contribution to permeability evolution as many other models, while also allowing for a pronounced permeability increase once plastic strain develops. Importantly, the transition to rapid permeability enhancement associated with the onset of dilatant pathways is triggered by a mechanical parameter, consistent with the interpretation that pathway formation is fundamentally a mechanically driven process.

5.4. Limitations and future works

A key limitation of the GT-experiment is that pore pressure was only monitored in the BGT-2 borehole, while no pore pressure data are available from the other observation boreholes. In particular, it would have been interesting to observe a pore pressure response in the boreholes that exhibited large strain changes, such as BGT-6. The only borehole in which both strain and pore pressure were recorded is BGT-2; however, the deformation signal predominantly propagated down-dip, and the FO cable in BGT-2 was not mounted directly to the rock but was installed in water and clamped to the packers. Such paired pressure-strain observations in the high-strain boreholes would have enabled a more direct comparison with earlier injection experiments, for example of Jockwer and Wieczorek.[7]

Another limitation is the large uncertainty in the in-situ stress field, as shown in Table 3. This becomes especially clear when compared with the HG-B experiment analyzed by Xu et al.,[30] which adopted a significantly different stress state despite being conducted at Mont Terri. The sensitivity of dilatant pathway formation and permeability enhancement to stress assumptions remains a major source of uncertainty.

Limitations are also associated with the permeability enhancement formulations used in this study. In the gas pressure-based approach, permeability enhancement is controlled directly by gas pressure rather than by a mechanical parameter. As a result, the model indirectly represents the effects of dilatant deformation, without explicitly resolving the mechanical processes responsible for permeability enhancement. While this simplified approach reproduces the observed pressure evolution reasonably well, it does not provide a fully coupled mechanical representation of dilatant pathway formation. In the strain-based approach, permeability enhancement is linked to plastic strain, which provides a more physically consistent representation of mechanically induced permeability changes. However, this approach also introduces a larger degree of freedom in the calibration parameters. Although a similar magnitude of permeability enhancement is required to reproduce the observed pressure drop, a broad trade-off exists between the introduced failure permeability value and the empirical parameter b_2, allowing multiple parameter combinations to produce comparable pressure responses. In addition, the degree of friction-angle softening influences stress redistribution and the rate at which the permeability-enhanced zone propagates through the model domain. In the present study, the softening behavior was calibrated using post-failure weakening behavior and was therefore not directly constrained by observations of dilatant processes themselves.

For future work, the modeling framework could account for more advanced constitutive laws. One option is an anisotropic-elasticity ubiquitous joint model, in which elastic parameters (e.g. Young's modulus, Poisson's ratio) are specified separately for the bedding and matrix. However, this constitutive model does not allow for strain softening in FLAC3D. Alternatively, the Cam–Clay model could better represent the elasto-plastic behavior of clay-rich rocks such as the Opalinus Clay. Benchmarking work within the DECOVALEX–2027 project (https://decovalex.org/) is focused on developing constitutive models for Opalinus Clay by reproducing the response observed in a range of laboratory experiments, with the longer-term objective of applying these models to simulations of dilatant gas flow. The constitutive formulations under development generally include anisotropic elastic behavior as well as strain hardening and softening to capture the progressive evolution from intact clay behavior to localized deformation. One of these constitutive models being used is the COMBA (Columnar-Basalt) model implemented in FLAC3D.[45–47] In the COMBA model, elastic anisotropy is represented through the stiffness of ubiquitous joints used to model bedding, while strain hardening/softening and preferential failure along weaker orientations (e.g. bedding planes or pre-existing joints) can be incorporated.

Regarding permeability enhancement formulations, future work could explore linking permeability more directly to dilatant pathway aperture, as proposed by Kim et al.[48] and Yang et al..[49] In the model of Kim et al.,[48] pathways are simulated by coupling TOUGH2 with a Rigid-Body-Spring Network (RBSN), enabling a discrete lattice representation of elasticity and fracture evolution. Yang et al.,[49] embedded fracture sets within a transversely isotropic constitutive model to represent bedding, with fracture aperture defined as a function of effective stress. In both approaches, permeability is controlled by evolving fracture aperture, providing a more mechanistic link between mechanical deformation and flow. These methods may offer valuable perspectives for refining future simulations of dilatant pathway development in the Opalinus Clay.

6. Conclusions

Gas transport through clay formations is a key process for assessing the long-term safety of deep geological repositories, where hydrogen may accumulate from corrosion. Large uncertainties remain regarding the onset of dilatant pathways, which may, under certain conditions, act as pressure-release mechanisms by allowing gas to escape before permanent fracturing occurs and repository integrity could be adversely affected.

In the GT-experiment at Mont Terri, helium injection into the Opalinus Clay over more than a year led to a sudden pressure drop of about 1 MPa, interpreted as the initiation of dilatant pathways. To investigate this, we carried out three numerical simulations: a TOUGH3-only fluid-flow model and two coupled hydro-mechanical models with permeability enhancement. The results indicate that gas transport was initially governed by two-phase flow with an elevated entry pressure, while the pressure drop corresponds to dilatant pathway formation that increases transmissivity by roughly two orders of magnitude. Comparisons with previous studies confirm that this behavior is consistent with dilatant pathways rather than hydrofracturing.

Both the pressure-based and strain-based permeability approaches reproduced the observed pressure response, but the strain-based method offers the advantage of being directly linked to the mechanical processes of pathway formation and enabling comparison with FO strain data. The FO data, together with earlier work, highlight the strong role of bedding planes in the initiation and evolution of dilatant pathways. While some discrepancies remain in the timing and magnitude of strain evolution, the approach provides valuable constraints for further model development.

Overall, even with simplified representations of permeability enhancement, our models capture the key processes observed during the GT-experiment and support the interpretation that dilatant pathway formation controls the sudden pressure drop. This study presents the first detailed modeling of a long-term in-situ gas injection experiment on the Opalinus Clay, with explicit focus on dilatant pathways and bedding-plane effects. Despite the challenges of modeling in-situ conditions, our results advance the understanding of gas flow in the Opalinus Clay and suggest that dilatant pathways may act as natural pressure-release mechanisms under repository-relevant conditions, thereby supporting the safety assessment of geological repositories.

CRediT authorship contribution statement

Matthijs Nuus: Writing – review & editing, Writing – original draft, Validation, Supervision, Software, Investigation, Formal analysis, Data curation, Conceptualization. **Antonio Pio Rinaldi:** Writing – review & editing, Supervision, Software, Resources, Project administration, Methodology, Investigation, Funding acquisition, Data curation, Conceptualization. **Robert Cuss:** Writing – review & editing, Resources, Project administration, Investigation, Funding acquisition, Conceptualization. **Manuel Sentis:** Writing – review & editing, Supervision, Resources, Project administration, Investigation, Funding acquisition, Conceptualization. **Bastian Graupner:** Writing – review & editing, Resources, Project administration, Investigation, Funding acquisition, Conceptualization. **Fabiano Magri:** Writing – review & editing, Investigation, Funding acquisition, Conceptualization. **Frédéric Bernier:** Writing – review & editing, Investigation, Funding acquisition, Conceptualization.

Declaration of Generative AI and AI-assisted technologies in the writing process

During the preparation of this work, the author(s) used ChatGPT to assist with text formatting and sentence structuring. The author(s) subsequently reviewed and edited the content as needed and take full responsibility for the content of the published article.

Declaration of competing interest

The authors declare that they have no known competing financial interests or personal relationships that could have appeared to influence the work reported in this paper.

Acknowledgments

The GT-experiment was made possible through the support of the Mont Terri Consortium project partners, including ENSI (CH), Swisstopo (CH), ETH Zürich (CH), FANC (BE), BASE (DE), BGR (DE) and SCK CEN (BE).

Appendix A. Supplementary data

Supplementary material related to this article can be found online at https://doi.org/10.1016/j.ijrmms.2026.106643.

Data availability

Research Link Provided

Dataset for coupled hydro-mechanical modeling of gas flow in Opalinus Clay (GT experiment) (Original data) (ETH Research Collection).

References

1. King F. Gaseous hydrogen issues in nuclear waste disposal. In: *Gaseous Hydrogen Embrittlement of Materials in Energy Technologies*. Elsevier; 2012:126–148.
2. Corkum A, Martin C. The mechanical behaviour of weak mudstone (opalinus clay) at low stresses. *Int J Rock Mech Min Sci*. 2007;44(2):196–209.
3. Kulenkampff J, Zakhnini A, Gründig M, Lippmann-Pipke J. Quantitative experimental monitoring of molecular diffusion in clay with positron emission tomography. *Solid Earth*. 2016;7(4):1207–1215.
4. Bagnoud A, Chourey K, Hettich RL, et al. Reconstructing a hydrogen-driven microbial metabolic network in opalinus clay rock. *Nat Commun*. 2016;7(1):12770.
5. Butterworth SJ, Barton F, Lloyd JR. Extremophilic microbial metabolism and radioactive waste disposal. *Extremophiles*. 2023;27(3):27.
6. Ruiz-Fresneda MA, Martinez-Moreno MF, Povedano-Priego C, Morales-Hidalgo M, Jroundi F, Merroun ML. Impact of microbial processes on the safety of deep geological repositories for radioactive waste. *Front Microbiol*. 2023;14:1134078.
7. Jockwer N, Wieczorek K. Gas migration in the opalinus clay as a function of the gas injection pressure. 2008 HG-C Project Report, GRS-249.
8. Marschall P, Horseman S, Gimmi T. Characterisation of gas transport properties of the opalinus clay, a potential host rock formation for radioactive waste disposal. *Oil & Gas Sci Technol*. 2005;60(1):121–139.
9. Harrington J, Horseman S. Gas transport properties of clays and mudrocks. *Geol Soc Lond Spec Publ*. 1999;158(1):107–124.
10. Rinaldi AP, Rutqvist J, Luu K, et al. TOUGH3-FLAC3D: a modeling approach for parallel computing of fluid flow and geomechanics. *Comput Geosci*. 2022;26(6):1563–1580.
11. Bossart P, Bernier F, Birkholzer J, et al. Mont terri rock laboratory, 20 years of research: introduction, site characteristics and overview of experiments. In: *Mont Terri Rock Laboratory, 20 years: Two Decades of Research and Experimentation on Claystones for Geological Disposal of Radioactive Waste*. Springer; 2018:3–22.
12. Mont Terri Project. Stratigraphie und fazies. 2024 URL https://www.mont-terri.ch/de/stratigraphie-und-fazies. [Accessed: 27 January 2025].
13. Cuss RJ, Gisiger J, Rinaldi AP, et al. The role of gas injection rate on the advective movement of gas in opalinus clay at the field scale. *Saf Nucl Waste Dispos Discuss*. 2026;2026:1–23.
14. Jung Y, Pau GSH, Finsterle S, Doughty CA. TOUGH3 user's guide, version 1.0. 2018.
15. Van Genuchten MT. A closed-form equation for predicting the hydraulic conductivity of unsaturated soils. *Soil Sci Am J*. 1980;44(5):892–898.
16. Luckner L, Van Genuchten MT, Nielsen D. A consistent set of parametric models for the two-phase flow of immiscible fluids in the subsurface. *Water Resour Res*. 1989;25(10):2187–2193.
17. NAGRA. *Production, Consumption and Transport of Gases in Deep Geological Repositories According to the Swiss Disposal Concept*. Technical Report 16–03; Switzerland: National Cooperative for the Disposal of Radioactive Waste (Nagra); 2016.
18. Itasca. *FLAC3D V6.0, Fast Lagrangian Analysis of Continua in 3 Dimensions, User's Guide*. Minneapolis, MN: Itasca Consulting Group; 2017.
19. Biot M. General three-dimensional theory of poroelasticity. *J Appl Phys*. 1941;12(2):155–164.
20. NAGRA. *Entsorgungsnachweis Für Abgebrannte Brennelemente, Verglaste Hochaktive Sowie Langlebige Mittelaktive Abfälle*. Technical Report 02–03; Nagra; 2002.
21. NAGRA. Effects of post-disposal gas generation in a repository for low- and intermediate-level waste sited in the opalinus clay of northern Switzerland. Technical Report 08–07; Nagra; 2008.
22. Guglielmi Y, Nussbaum C, Rutqvist J, Cappa F, Jeanne P, Birkholzer J. Estimating perturbed stress from 3-D borehole displacements induced by fluid injection in fractured or faulted shales. *Geophys J Int*. 2020;221(3):1684–1695.
23. Amann F, Wild KM, Loew S, Yong S, Thoeny R, Frank E. Geomechanical behaviour of opalinus clay at multiple scales: results from mont terri rock laboratory (Switzerland). In: *Mont Terri Rock Laboratory, 20 Years: Two Decades of Research and Experimentation on Claystones for Geological Disposal of Radioactive Waste*. Springer; 2018:153–173.
24. Sciandra D, Kivi IR, Vilarrasa V, Makhnenko RY, Rebscher D. Hydro-mechanical response of opalinus clay in the CO2 long-term periodic injection experiment (CO2lpie) at the mont terri rock laboratory. *Geomech Geophys Geo-Energy Geo-Resources*. 2022;8(5):166.
25. NAGRA. *SGT Etappe 2, Vorschlag Weiter Zu Untersuchender Geologischer Standortgebiete Mit Zugehörigen Standortarealen Für Die Oberflächenanlage – Geologische Grundlagen – Geomechanische Unterlagen*. Technical Report NTB 14-02, Dossier IV; Nagra; 2014.

26. Salzer T, Popp K. *HE-D experiment: Influence of bedding planes*. Unpublished Mont Terri Technical Report 2007-04; Switzerland: Mont Terri Project; 2007.
27. Haug C. Mechanische charakterisierung prä-existenter tektonischer trennflächen im opalinuston. 2009.
28. Amann F, Button EA, Blümel M, Thöny R. Insight into the mechanical behavior of opalinus clay. 2010.
29. Senger R, Lanyon B, Marschall P, Vomvoris S, Fujiwara A. Numerical modeling of the gas migration test at the grimsel test site (Switzerland). *Nucl Technol*. 2008;164(2):155–168.
30. Xu W, Shao H, Hesser J, Wang W, Schuster K, Kolditz O. Coupled multiphase flow and elasto-plastic modelling of in-situ gas injection experiments in saturated claystone (Mont Terri Rock Laboratory). *Eng Geol*. 2013;157:55–68.
31. Kim J, Sonnenthal EL, Rutqvist J. Formulation and sequential numerical algorithms of coupled fluid/heat flow and geomechanics for multiple porosity materials. *Internat J Numer Methods Engrg*. 2012;92(5):425–456.
32. Geuzaine C, Remacle J-F. Gmsh: A 3-D finite element mesh generator with built-in pre-and post-processing facilities. *Internat J Numer Methods Engrg*. 2009;79(11):1309–1331.
33. Cuss R, Harrington J, Giot R, Auvray C. Experimental observations of mechanical dilation at the onset of gas flow in callovo-oxfordian claystone. *Geol Soc Lond Spec Publ*. 2014;400:507–519. http://dx.doi.org/10.1144/SP400.26,
34. Winhausen L, Khaledi K, Jalali M, Bretthauer M, Amann F. The anisotropic behavior of a clay shale: Strength, hydro-mechanical couplings and failure processes. *J Geophys Res: Solid Earth*. 2023;128(11):e2023JB027382.
35. Ismael M, Konietzky H, Herbst M. A new continuum-based constitutive model for the simulation of the inherent anisotropy of opalinus clay. *Tunn Undergr Space Technol*. 2019;93:103106.
36. Konietzky H, Blümling P, te Kamp L. *Opalinuston, Felsmechanische Untersuchungen*. Technical Report Nagra Interne Berichte (NIB) 03-08; Nagra; 2003.
37. Popp T, Salzer K. *HE-D Experiment: Influence of Bedding Planes (IfG) - Final Report*. Technical Report 2007-04; Mont Terri Project; 2007.
38. Bock H. *RA Experiment: Updated Review of the Rock Mechanics Properties of the Opalinus Clay of the Mont Terri URL Based on Laboratory and Field Testing*. Technical Report 2008-04; Mont Terri Project; 2009.
39. Thöny R. *Geomechanical Analysis of Excavation-Induced Rock Mass Behavior of Faulted Opalinus Clay at the Mont Terri Underground Rock Laboratory (Switzerland)* [Ph.D. thesis]. ETH Zurich; 2014.
40. Bock H. *RA Experiment: Data report on rock mechanics-Mont Terri project*. NAGRA Technical Report TN00-02; 2000.
41. Radeisen E. *Numerical Modeling of Pressure-Induced Advective Gas Flow Through Dilatant Pathways in Saturated Claystone and Bentonite Using Coupled Multiphase Flow and Strain-Dependent Material Properties* [Ph.D. thesis]. Technische Universität Dresden; 2024 URL https://nbn-resolving.org/urn:nbn:de:bsz:14-qucosa2-936763.
42. Rutqvist J, Wu Y-S, Tsang C-F, Bodvarsson G. A modeling approach for analysis of coupled multiphase fluid flow, heat transfer, and deformation in fractured porous rock. *Int J Rock Mech Min Sci*. 2002;39(4):429–442.
43. Olivella S, Alonso E. Gas flow through clay barriers. *Géotechnique*. 2008;58(3):157–176.
44. Zhu W, Wei C. Numerical simulation on mining-induced water inrushes related to geologic structures using a damage-based hydromechanical model. *Environ Earth Sci*. 2011;62(1):43–54.
45. Itasca Consulting Group, Inc. *FLAC3D — Fast Lagrangian Analysis of Continua in Three-Dimensions*. Version 9.0 ed. Minneapolis, MN: Itasca Consulting Group, Inc.; 2023.
46. Detournay C, Meng G, Cundall P. Development of a constitutive model for columnar basalt. In: *Proceedings of the 4th Itasca Symposium on Applied Numerical Modeling, Lima, Peru*. 2016:249–265.
47. Meng G, Detournay C, Cundall P. Formulation and application of a constitutive model for multijointed material to rock mass engineering. *Int J Geomech*. 2020;20(6):04020044.
48. Kim K, Rutqvist J, Harrington JF, Tamayo-Mas E, Birkholzer JT. Discrete dilatant pathway modeling of gas migration through compacted bentonite clay. *Int J Rock Mech Min Sci*. 2021;137:104569.
49. Yang J, Fall M, Guo G. A three-dimensional hydro-mechanical model for simulation of dilatancy controlled gas flow in anisotropic claystone. *Rock Mech Rock Eng*. 2020;53(9):4091–4116.